Remote Sensing of Environment 122 (2012) 146–165

Contents lists available at SciVerse ScienceDirect

Remote Sensing of Environment

journal homepage: www.elsevier.com/locate/rse

Using Landsat-derived disturbance history (1972–2010) to predict current forest structure

Dirk Pflugmacher [a,*], Warren B. Cohen [b], Robert E. Kennedy [a]

[a] Department of Forest Ecosystems and Society, Oregon State University, 321 Richardson Hall, Corvallis, OR 97331, USA
[b] USDA Forest Service, Pacific Northwest Research Station, Forestry Sciences Laboratory, 3200 SW Jefferson Way, Corvallis, OR 97331, USA

ARTICLE INFO

Article history:
Received 3 May 2011
Received in revised form 16 August 2011
Accepted 8 September 2011
Available online 23 February 2012

Keywords:
Landsat
Time series
Forest disturbance
Biomass
Carbon
Lidar
MSS
Tasseled cap
LandTrendr
TimeSync

ABSTRACT

Lidar is currently the most accurate method for remote estimation of forest structure, but it has limited spatial and temporal coverage. Conversely, Landsat data are more widely available, but exhibit a weaker relationship with structure under medium to high leaf area conditions. One potentially valuable means of enhancing the relationship between Landsat reflectance and forest structure is to incorporate Landsat spectral trends prior to a date of interest. Because the condition of a forest stand at any point in time is linked to the stand's disturbance history, an approach that directly leverages the temporal information of Landsat time series should improve estimates of forest structure. The main objective of this study was to test and demonstrate the utility of disturbance and recovery metrics derived from spectral profiles of annual Landsat time series (LTS) to predict current forest structure attributes (as compared to more traditional approaches, including airborne, discrete return lidar and single-date Landsat). We estimated aboveground live biomass (AGB_{live}), dead woody biomass (AGB_{dead}), basal area (live and dead), and Lorey's mean stand height for a mixed-conifer forest in eastern Oregon, USA, and compared the results with estimates from lidar and single, current-date Landsat imagery. Annual time-series stacks for the entire Landsat record (1972–2010) were obtained to characterize all long-term (insect, growth) and short-term (fire, harvest) vegetation changes that occurred during that period. This required the additional objective of integrating Landsat data from MSS and TM/ETM+ sensors, and we describe here our approach. To extract spectral trajectories and change metrics associated with forest disturbances and recovery we applied a temporal segmentation to the calibrated time series.

Lidar predicted forest structure of live trees most accurately (e.g. AGB_{live}: $R^2 = 0.88$, RMSE = 35.3 Mg ha^{-1}). However, LTS metrics significantly improved model predictions (e.g. AGB_{live}: $R^2 = 0.80$, RMSE = 46.9 Mg ha^{-1}) compared to single-date Landsat data (AGB_{live}, $R^2 = 0.58$, RMSE = 65.1 Mg ha^{-1}). Conversely, distributions of AGB_{dead} were more strongly associated with disturbance history than current structure of live trees. As a result, LTS models performed significantly better in estimating AGB_{dead} ($R^2 = 0.73$, RMSE = 31.0 Mg ha^{-1}), than lidar models ($R^2 = 0.21$, RMSE = 43.8 Mg ha^{-1}); and single-date Landsat data failed completely ($R^2 = 0$, RMSE = 47.8 Mg ha^{-1}). Further, LTS metrics that integrated disturbance and recovery history over the entire time series generally predicted AGB_{dead} better than metrics describing single events only (e.g. the greatest disturbance). This study demonstrates the unique value of the long, historic Landsat record, and suggests new potentials for mapping current forest structure with Landsat.

1. Introduction

Accurate spatial estimates of forest structure are required for a broad range of ecological applications including studies of the terrestrial carbon cycle (Houghton, 2005) and research on wildlife habitat and biodiversity (Bergen et al., 2009). Because forest structure is highly variable in space and time, there is great interest in estimating key parameters using remote sensing. Lidar is currently the most accurate sensor technology to achieve this task. There are numerous studies that have demonstrated that lidar can accurately estimate forest height and aboveground biomass (Drake et al., 2003; Lefsky et al., 1999), and a variety of other ecologically imporant variables such as leaf area index (Zhao & Popescu, 2009), vertical vegetation strata (Morsdorf et al., 2010), succession stages (Falkowski et al., 2009), and canopy structure (Andersen et al., 2005; Lefsky et al., 2005a). As a result, the availability of airborne lidar data is rapidly increasing, but the costs associated with acquisition, data storage and processing are high. Lidar data from spaceborne sensors that meet the measurement requirements for vegetation studies (Hall et al., 2011)) will not be available in the near future. Therefore, alternative approaches that include other remote sensing data, e.g. passive optical, are needed.

* Corresponding author. Tel.: +1 541 750 7287; fax: +1 541 737 1393.
E-mail address: dirk.pflugmacher@oregonstate.edu (D. Pflugmacher).

0034-4257/$ – see front matter © 2012 Elsevier Inc. All rights reserved.
doi:10.1016/j.rse.2011.09.025

Estimating forest structure variables with Landsat and other multi-spectral sensors has been a research topic of great interest (e.g. Cohen & Spies, 1992; Hall et al., 2006; Powell et al., 2010). The advantages of Landsat are several, including a spatial resolution that captures the fine-grained patterns of land-cover and land-use change associated with land management, a long history of widespread use and acceptance (Cohen & Goward, 2004), and a data record going back to 1972. However, the sensitivity of Landsat and other passive optical sensors to discriminate vertical structure is limited (e.g. Lu, 2006); the signal recorded by these sensors is known to saturate in high leaf-area forests (Turner et al., 1999).

Current forest structure and composition is a function of disturbance history (Harmon et al., 1990; Spies, 1998). Type and intensity of disturbance events (e.g. insect, fire, and harvest) affect the amount of dead woody material produced, and by extension the amount of live biomass left following disturbance. Bark beetle outbreaks can cause widespread tree mortality that may become a large contiguous fuel base for subsequent fires (Parker et al., 2006). Frequency and intensity of disturbances affect carbon storage not only through the production of dead woody material, but also by affecting forest productivity when nutrient availability is limited (Gough et al., 2008). The concept that forest structure is influenced by disturbances and environmental conditions, and can be described through ecological processes of tree growth, mortality, and decomposition, is commonly applied in forest yield and ecosystem process models (Landsberg & Waring, 1997; Thornton et al., 2002). In fact, forest management utilizes these concepts to achieve specific, desirable structural conditions, either for wood production or other ecosystem services such as wildlife habitat. By means of silvicultural treatments such as harvest, planting, herbicide application, prescribed fire, humans alter forests in ways that lead to specific prescribed conditions (O'hara, 2001).

It follows that if sufficient spatial data of the disturbance and regrowth history can be obtained then this information could be used to map the current condition of forest stands for which structural information is unavailable or incomplete. There is growing consensus that dense time-series records are required to accurately monitor forest change in dynamic systems (Lunetta et al., 2004). However, it is less clear what kind of change metrics need to be observed to accurately characterize current forest conditions. Because forest age is a primary driver of forest structure in homogenous and managed forests, time since disturbance is frequently being used as a surrogate to predict structure (Helmer et al., 2010; Lefsky et al., 2005b). However, partial disturbances from fire, insect, and logging can lead to more complex systems of uneven age-structure. Rates of forest regeneration after disturbances can be highly variable even for relatively homogeneous coniferous forests within similar site conditions (Yang et al., 2005). One potential way to improve on single age-related predictors is to quantify disturbance and regrowth trends across the full Landsat record and include information not only related to stand-replacing disturbances but also to long-term changes in vegetation cover (Kennedy et al., 2010).

Landsat's data record makes it well suited for mapping forest change, and there have been numerous studies on this topic. Disturbance characterization has been the most common usage of the Landsat archive (Cohen et al., 2002; Huang et al., 2010; Masek et al., 2008), with specific emphases on harvest and fire (Roder et al., 2008; Schroeder et al., 2011), insects (Meigs et al., 2011; Goodwin et al., 2008; Wulder et al., 2005), and forest loss due to land use conversion (Powell et al., 2008). Other studies have used the Landsat archive for the purpose of understanding recent trajectories of forest succession, including both primary (Lawrence & Ripple, 2000) and secondary succession (Peterson & Nilson, 1993; Jakubauskas, 1996; Schroeder et al., 2007; Gómez et al., 2011). However, the focus of most studies that used Landsat time-series has been to quantify historic changes for retrospective analyses (e.g., Healey et al., 2008; Kuemmerle et al., 2009) or as baseline information to establish potential future scenarios (e.g. Baker et al., 2004; Spies et al., 2007). There are studies that have used multi-temporal Landsat data to detect stand replacing disturbances, and then estimate forest structure from the timing of disturbance (which is related to forest age in some systems as mentioned above) (Helmer et al., 2010; Lefsky et al., 2005b). However, there have been no studies that use the long-term data record at an approximately annual time step to map current forest conditions by explicitly incorporating Landsat-derived forest disturbance and recovery trends in predictive models.

Recent improvements of Landsat MSS data products support studies of historical vegetation trends back to the early 1970s. The release of the long-term Landsat archive for free (Woodcock et al., 2008) opened new opportunities to detect long-term vegetation changes with dense time series (Huang et al., 2010; Kennedy et al., 2010; Sonnenschein et al., 2011), but to-date only few time-series studies have utilized MSS imagery (Hostert et al., 2003; Powell et al., 2008; Gómez et al., 2011). However, recent developments could greatly enhance the utility of MSS imagery for time-series analyses. In fall 2010, the USGS released new MSS data products with improved radiometry and geometric correction (http://landsat.usgs.gov/NewMSSProduct.php). MSS data are now processed with the Level 1 Product Generation System (LPGS), similar to TM and ETM+, and are cross-calibrated to improve radiometric consistency across sensors. In addition, the majority of imagery is now available as terrain-corrected product (L1T).

In this study, we test the hypothesis that Landsat disturbance history is a good predictor of current forest structure by exploring empirical relationships between field-measurements of current forest structure and disturbance and recovery trajectories derived from spectral profiles of annual Landsat time series. Forest structure can be described in numerous ways (Spies, 1998). Here, we focus on a few, representative metrics: aboveground tree biomass, basal area and height. Because lidar is the 'gold standard' for remote detection of forest structure, and because single-date Landsat data have been exhaustively studied for this problem, we compare the results from Landsat time series with results from these two other datasets. Our objectives were to:

- Characterize forest disturbance history through the full temporal depth of the Landsat archive. This required integration of MSS and TM/ETM+ data into a single, normalized time series to obtain annual Landsat observations between 1972 and 2010. For our approach, it was necessary to improve MSS geometric registration relative to TM/ETM+, derive new tasseled cap coefficients for MSS data, and conduct scene-level radiometric normalization and pixel-level spectral index alignment.
- Derive and evaluate prediction models, for a variety of forest structure variables, from Landsat time series, lidar, and single-date Landsat. Aboveground live biomass is an important variable for linkage with ecosystem models, but we include others, like basal area (BA) and height, which are important for forest management. Because dead wood is important for a variety of wildlife, fire behavior, and related models that are based on comprehensive ecosystem functional descriptions, we also examine predictability of aboveground dead wood.

2. Methods

2.1. Study area

The study area is located in the Blue Mountains of eastern Oregon, USA, and covers an area of ~830 km^2 (Fig. 1). The region is dry, with a large range of average annual precipitation from 305 mm to 1270 mm. Elevation ranges between 500 m and 2700 m. Forest types include spruce (*Picea engelmannii* Parry ex Engelm.) and grand fir (*Abies grandis* [Douglas ex D. Don] Lindl.) at the higher

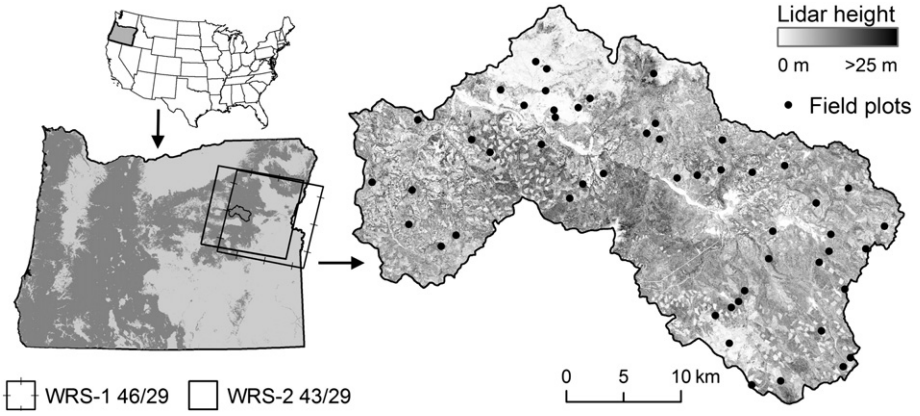

Fig. 1. Study area in Oregon, USA, location of field plots, and lidar canopy height surface.

elevations, mixed conifer at mid elevations, and ponderosa pine (*Pinus ponderosa* Douglas ex P. Lawson & C. Lawson) at lower elevations (Franklin & Dyrness, 1988). Hardwood species such as black cottonwood (*Populus trichocarpa* Torr. & Gray), quaking aspen (*Populus tremuloides* Michx.), and willow (*Salix* spp.) occur mainly in the riparian areas and wetlands. Current forest structure of the area has been shaped by natural and anthropogenic disturbances, with harvest, insects, and fire as major components. Mountain pine beetle (*Dendroctonus ponderosae* Hopkins) and western spruce budworm (*Choristoneura occidentalis* Freeman) are the main causes of insect defoliation and mortality. Thinning harvest and frequent low intensity fire are common, which have created structurally and compositionally complex mixed and multi-aged conifer-dominated forests (Campbell et al., 1996).

2.2. Field sampling

Fifty-one plots were located across the study area using a stratified systematic sampling protocol (Fig. 1). We stratified the study area using a combination of lidar median canopy height and Landsat Normalized Burn Ratio (NBR, Key & Benson, 2005) for the year 2008. Using the Jenks Natural Breaks Classification in ArcGIS 9.3 (ESRI, Inc.), the median canopy height distribution was grouped into 4 classes (0.5–5.2 m, 5.3–10.7 m, 10.8–15.4, 15.5–23.2) and the NBR distribution was grouped into 5 classes (−0.3–0.12, 0.13–0.25, 0.26–0.37, 0.38–0.48, 0.49–0.76). The Jenks method determines class breaks by minimizing within class variance and maximizing differences between classes. Field plots were randomly selected and equally distributed across the canopy height and NBR classes, respectively. Because lidar height is related to forest structure (Lefsky et al., 2005a,b) and NBR (like most spectral indices) is related to forest cover, employing these strata ensured that the plots covered a range of current forest structure and cover conditions. Field data were collected during summer 2009 using a fixed, 15-m radius at each plot. The location of each plot center was recorded using a Trimble GeoXM GPS. Average horizontal precision of plot coordinates after differential correction was 2.6 m (±1.1 m).

2.2.1. Field data

Within each plot, diameter at breast height (dbh), species, height, decay class, and the height of broken tops were recorded for live and dead trees with dbh > 2.5 cm. For selected trees, we also measured the distance and bearing from the plot center. Tree heights were measured using a Haglöf Laser Vertex Hypsometer. We estimated total aboveground (oven-dry weight) biomass for all trees from a set of 10 allometric equations developed for regional studies (Jenkins et al., 2003). The Jenkins equations distinguish between four hardwood and six softwood species groups and use a simple log-linear regression model with tree diameter (dbh) as the predictor variable.

Biomass for standing dead trees including snags greater than 1.3 m height was estimated by adjusting total tree biomass estimates for live trees using component ratio equations from Jenkins et al. (2003). The component equations estimate the proportion of total aboveground biomass in a given biomass component (wood, bark, foliage). Total biomass in branches and treetops was calculated from the differences between total biomass and the sum of the individual components. Analogous to Smith et al. (2003), we reduced the mass of intact standing dead relative to live by the following amounts: 10% of stem wood and bark, 100% of leaves, and 33% of branches. For trees with broken tops we estimate the total tree height by fitting a Lundqvist function (Moore et al., 1996) for each tree species to the diameter and height of measured live intact trees. Then, we calculated the ratio of actual tree volume to total tree volume based on estimated total tree height using formulas for the frustum of a cone with a top diameter of 2.5 cm. Finally, the ratio of actual to total bole volume was used to further reduce stem wood and bark biomass of dead trees with broken tops.

We calculated total dead biomass by adding together biomass of standing dead trees and biomass of down wood. We measured down woody debris at each plot with the line-intercept method (Harmon & Sexton, 1996; Van Wagner, 1968; Warren & Olsen, 1964), using two orthogonal line-transects crossing at the plot center and pointing towards magnetic north and east, respectively. We recorded species, decay class (Waddell, 2002) and diameter of each down log with diameter > 10 cm. Volume was calculated after Van Wagner (1968):

$$V = \pi^2 \cdot \sum d^2 / 8L \quad (1)$$

where V is the volume per unit area ($m^3\ m^{-2}$), d is the piece diameter (m), and L is the transect length (m). Volume estimates were converted to biomass using species-specific wood densities from Jenkins et al. (2003) and decay-class-specific density reduction factors from Waddell (2002).

In addition to biomass, we estimated basal area ($m^2\ m^{-2}$) of live and dead trees and stand height for live trees (Table 1). As a measure of stand height we calculated Lorey's mean height (Lorey, 1878), which reflects more closely the height of the dominant tree stratum in multi-layer canopies compared to the standard mean height. The Lorey height weights the contribution of trees to the stand by their basal area as follows:

$$H_L = \frac{\sum g \cdot h}{\sum g} \quad (2)$$

where g and h represent basal area and height of all measured trees within a plot, respectively.

Table 1
Number of plots, mean stand height, basal area of live and dead trees, and biomass of live trees and dead wood grouped by disturbance agent of the greatest disturbance between 1972 and 2010 (standard deviation = SD).

Type of greatest disturbance	Number of plots	Mean stand height (SD) (m)	Mean live basal area (SD) (m^2 ha^{-1})	Mean dead basal area (SD) (m^2 ha^{-1})	Mean live AGB (SD) (Mg ha^{-1})	Mean dead AGB (SD) (Mg ha^{-1})
Fire	8	4.6 (6.1)	2.8 (5.2)	8.5 (12.2)	11.8 (26.7)	65.4 (77.2)
Harvest	14	17.6 (5.8)	15.7 (7.9)	1.5 (1.9)	79.5 (52.1)	19.9 (15.4)
Insect-Pathogen	8	21.3 (6.5)	33.4 (12.2)	10.1 (14.2)	189.3 (113.9)	71.7 (59.5)
Undisturbed	21	19.3 (6.9)	27.3 (13.3)	2.2 (2.9)	147.0 (94.0)	19.4 (20.9)

2.3. Lidar

Discrete return lidar data for the entire study area were acquired between 19 and 28 August 2008 using a Leica ALS50 Phase II laser system mounted in Cessna Caravan 208B (Table 2). The lidar system recorded range and intensity of up to 4 returns per pulse, and achieved a nominal pulse density of >8 pulses per m^2. Data delivered by the vendor included a digital elevation model (DEM) of 1-m spatial resolution. To obtain estimates of aboveground height for each return, we subtracted the DEM elevation from the point elevations.

We extracted all lidar returns co-located with our field plots, and computed 26 potential predictor variables from the height and intensity distributions of each plot (Table 3). Returns above a threshold of 0.5 m were considered vegetation returns, and returns below that threshold were considered ground returns. Height metrics included all recorded returns per pulse, whereas only first returns were used to compute intensity metrics. Height metrics were selected to characterize top (HMAX) and average vegetation height (HMEAN, HPEAK), vegetation density (CANCOV, RPC1), volume fraction (HVOL), and shape (HKURT and HSKEW) and variability (HCV, HSD, and HCV75) of the vertical distribution of vegetation. CANCOV was calculated by dividing the number of all returns above 2-m by the total number of returns including ground returns. We found that CANCOV calculated from all returns explained slightly more variation in forest biomass than when only first returns were used, albeit the difference was minimal. We therefore report here only results based on all returns. To obtain HVOL we multiplied CANCOV by HMEAN (Kim et al., 2009). Intensity metrics included mean (IMEAN and IMEAN75), maximum (IMAX), standard deviation (ISD) and shape of the vegetation intensity (ISKEW and IKURT). We did not correct lidar intensity for variable gain or range differences. However, visual inspection of the mean intensity raster revealed no significant terrain or flight line patterns. Finally, we derived percentile metrics from the relative frequency distributions of vegetation heights and return intensities. Lidar metrics were computed using the R-language (R Development Core Team, 2011).

2.4. Landsat

2.4.1. Geometric reprocessing of MSS

Table 2
Lidar data acquisition parameters.

Sensor	Leica ALS50 Phase II
Acquisition date	19–28 August, 2008
Flight altitude	900 m above ground
Flight line sidelap	50%
Maximum off-nadir scan angle	±14° from nadir
Returns/pulse	Up to 4
Density	>8 pulses m^{-2}
Pulse repetition	>105 kHz
Laser wavelength	1064 nm

From the Landsat archive (http://glovis.usgs.gov/) we obtained annual, near-anniversary date Landsat images of the study area acquired between mid-July and August from 1972 to 2010 (Table 4). All of the TM and ETM+ data and most of the MSS data (80%) were delivered terrain corrected (L1T). However, the terrain corrected MSS imagery showed lower geometric accuracy than the TM/ETM+ data. About 63% of the L1T MSS data had reported scene-wide root mean square error (RMSE) greater than 1 pixel (60 m). To improve the accuracy of the time series analysis we co-registered all MSS imagery to a reference TM image using an automated tie-point program (Kennedy & Cohen, 2003) and 2nd-order polynomial transformations. To match the spatial resolution of the TM and ETM+ data we resampled the MSS imagery to 30 m. Co-registration was performed on the entire scene overlap. Images with RMSEs greater than 0.5 pixels were removed from the analysis leaving a stack of annual Landsat imagery except for the years 1974, 1976, and 1982. The 1982-image was removed because it had been acquired late in the year (October). Limiting the choice of imagery to a relatively narrow mid-summer period minimized inter-annual variations caused by changes in vegetation phenology and sun-illumination conditions.

2.4.2. MSS tasseled cap revisited

The tasseled cap (TC) is a linear transformation of Landsat's spectral bands that was originally developed for Landsat MSS (Kauth & Thomas, 1976; Kauth et al., 1979) and later adapted for Landsat TM (Crist & Cicone, 1984), and ETM+ (Huang et al., 2002). The transformation yields a set of orthogonal components: brightness (TCB), greenness (TCG), and wetness (TCW), whereas TCW is not defined for MSS data. The TC components have been widely used to characterize vegetation conditions (Cohen & Goward, 2004) and for studying forest change (Cohen et al., 2002; Healey et al., 2005; Wulder, et al., 2004). The MSS tasseled cap is a DN-based (digital number) transformation, and therefore specific to the post-calibration coefficients used to rescale the calibrated radiance data to calibrated DN. Starting September 15th 2010, the USGS EROS switched the processing of the MSS archive to LPGS resulting in new post-calibration dynamic ranges and data quantization that are significantly different from the ones previously used. Because of these changes, the tasseled cap transformation cannot be directly applied to the new MSS data without adjusting for the differences in the band-specific rescaling factors. Following Hay (1991) and Parris and Rice (1983), we computed new MSS tasseled cap coefficients that matched the current post-calibration coefficients by converting the original tasseled cap rotation matrix for Landsat 2 (Kauth et al., 1979; Thompson & Wehmanen, 1980) using earlier post-calibration coefficients from Markham and Barker (1986). Our adjustments also accounted for variations in exoatmoshperic irradiance and those values were obtained from Chander et al. (2009).

To convert between calibrated radiance and calibrated DN values we first calculated band-specific rescaling gain and bias factors as follows:

$$L = B + G \cdot Q \quad (2)$$

Table 3
Lidar metrics derived from plot-level distributions of pulse return heights and intensities and their correlation coefficients with field measurements. Variables marked with an asterisk were correlated with other (more informative) predictor variables ($r > 0.9$) and excluded from the regression analyses. Shading illustrates the strength of the correlation independent of the sign: from 0 (white) to −1 and 1 (gray).

Variable	Description	AGB live	AGB dead	Basal area live	Basal area dead	Lorey height
HMAX*	Height, maximum of vegetation returns	0.67	0.18	0.65	0.20	0.75
HMEAN*	Height, mean of vegetation returns	0.85	0.00	0.85	0.09	0.91
HMEDIAN	Height, median of vegetation returns	0.84	–0.10	0.85	0.00	0.92
HPEAK	Height, height of upper mode	0.37	0.20	0.32	0.19	0.42
HCV	Height, coefficient of variation of vegetation returns	–0.51	0.22	–0.59	0.12	–0.58
HCV75	Height, coefficient of variation of upper 75 percentile	–0.54	0.25	–0.63	0.23	–0.72
HSD	Height, standard deviation of vegetation returns	0.46	0.35	0.42	0.29	0.55
HSKEW	Height, skewness of vegetation returns	–0.58	0.07	–0.65	–0.04	–0.71
HKURT	Height, kurtosis of vegetation returns	–0.37	–0.04	–0.43	–0.13	–0.50
H05PCT	Hei ght, 5th percentile of vegetation returns	0.59	–0.20	0.62	–0.07	0.58
H25PCT*	Height, 25th percentile of vegetation returns	0.81	–0.13	0.82	–0.01	0.87
H75PCT*	Height, 75th percentile of vegetation returns	0.81	0.00	0.82	0.06	0.90
H95PCT	Height, 95th percentile of vegetation returns	0.74	0.18	0.71	0.21	0.81
CANCOV	Vegetation returns >2 m*100/total returns	0.80	–0.13	0.89	–0.05	0.76
HVOL	CANCOVxHMEAN / 100	0.94	–0.06	0.94	0.02	0.83
RPC1	Percentage of 1st returns to all returns	–0.70	0.11	–0.81	0.03	–0.74
IMAX	Intensity, maximum of first returns	0.06	–0.02	0.14	0.00	0.12
IMEAN	Intensity, mean of first returns	–0.34	0.03	–0.47	–0.01	–0.19
ISD	Intensity, standard deviation of vegetation returns	0.60	–0.09	0.71	–0.05	0.78
ISKEW	Intensity, skewness of vegetation returns	0.37	–0.08	0.49	–0.07	0.23
IKURT*	Intensity, kurtosis of vegetation returns	–0.62	0.13	–0.71	0.08	–0.77
I25PCT*	Intensity, 25th percentile	–0.61	0.06	–0.73	0.01	–0.58
I50PCT*	Intensity, 50th percentile	–0.31	0.03	–0.45	0.00	–0.14
I75PCT	Intensity, 75th percentile	0.04	–0.02	–0.02	–0.05	0.29
I95PCT	Intensity, 95th percentile	0.27	–0.09	0.36	–0.11	0.50
IMEAN75	Intensity, mean above 75th percentile of height distribution	0.39	–0.44	0.39	–0.32	0.43

$$G = \frac{LMAX - LMIN}{QCALMAX - QCALMIN} \quad (3)$$

$$B = LMIN - G \cdot QCALMIN \quad (4)$$

where,

L spectral radiance at the sensor's aperture [W/(m^2 sr μm)]
Q quantized calibrated pixel value [DN]
G band-specific rescaling gain factor [(W/(m^2 sr μm))/DN]
B band-specific rescaling bias factor [W/(m^2 sr μm)]
QCALMIN minimum quantized calibrated pixel value corresponding to $LMIN_\lambda$ [DN]
QCALMAX maximum quantized calibrated pixel value corresponding to $LMAX_\lambda$ [DN]
LMIN spectral at-sensor radiance that is scaled to QCALMIN [W/(m^2 sr μm)]
LMAX spectral at-sensor radiance that is scaled to QCALMAX [W/(m^2 sr μm)]

The post-calibration dynamic ranges and rescaling factors of the input and reference data are shown in Table 5. To convert between DN values of current MSS data (input) and DN values of Landsat 2 data before 7/16/1975 (reference), we computed adjusted band-specific rescaling factors while accounting for variations in exoatmospheric irradiance (ESUN). For the Landsat 2 reference we used ESUN values for Landsat 2. Because MSS data from the USGS were cross-calibrated to Landsat 5 MSS, ESUN values for Landsat 5 MSS were used for all MSS images. In the following equations, subscripts R and I denote coefficients from the reference and input data set, respectively.

$$Q_R = \frac{G_I}{G_R} E \cdot Q_I + \frac{E \cdot B_I - B_R}{G_R} \quad (5)$$

$$E = \frac{ESUN_R}{ESUN_I} \quad (6)$$

$$G_A = \frac{G_I}{G_R} E \quad (7)$$

$$B_A = \frac{E \cdot B_I - B_R}{G_R} \quad (8)$$

where,

ESUN band-specific mean solar exoatmospheric spectral irradiance [W/m^2 μm]

Table 4
Acquisition date and Landsat sensor of the images used in this study. The 1997 geometric and MADCAL reference image is denoted by an asterisk. Images from 1972 to 1981 are referenced to WRS-1 path 46, row 29. Images between 1983 and 2010 are referenced to WRS-2 path 43, row 29.

Year	Date	Satellite
1972	08/12	Landsat 1 MSS
1973	08/07	Landsat 1 MSS
1975	08/15	Landsat 1 MSS
1977	08/13	Landsat 2 MSS
1978	07/30	Landsat 3 MSS
1979	08/03	Landsat 2 MSS
1980	08/16	Landsat 2 MSS
1981	08/10	Landsat 2 MSS
1983	07/04	Landsat 4 MSS
1984	07/14	Landsat 5 MSS
1984	07/14	Landsat 5 TM
1985	07/17	Landsat 5 MSS
1985	07/17	Landsat 5 TM
1986	07/20	Landsat 5 MSS
1986	07/20	Landsat 5 TM
1987	08/08	Landsat 5 MSS
1987	08/08	Landsat 5 TM
1988	07/25	Landsat 5 TM
1988	08/10	Landsat 5 MSS
1989	07/28	Landsat 5 TM
1989	08/05	Landsat 4 MSS
1990	07/31	Landsat 5 MSS
1990	08/16	Landsat 5 TM
1991	07/18	Landsat 5 TM
1992	08/05	Landsat 5 MSS
1992	08/05	Landsat 5 TM
1993	08/08	Landsat 5 TM
1994	07/26	Landsat 5 TM
1995	08/14	Landsat 5 TM
1996	07/31	Landsat 5 TM
1997*	08/03	Landsat 5 TM
1998	07/21	Landsat 5 TM
1999	07/08	Landsat 5 TM
2000	08/11	Landsat 5 TM
2001	08/06	Landsat 7 ETM+
2002	08/09	Landsat 7 ETM+
2003	08/20	Landsat 5 TM
2004	07/21	Landsat 5 TM
2005	07/24	Landsat 5 TM
2006	07/27	Landsat 5 TM
2007	07/30	Landsat 5 TM
2008	08/01	Landsat 5 TM
2009	07/19	Landsat 5 TM
2010	08/07	Landsat 5 TM

G_A adjusted band-specific rescaling gain factor [(W/(m^2 sr μm))/DN]

B_A adjusted band-specific rescaling bias factor [(W/(m^2 sr μm))/DN].

The adjusted rescaling gain and bias factors can be used to convert pixel values (DN) of recent MSS data to pixel values (DN) of the Landsat 2 reference data. The Landsat 2 tasseled cap coefficients can then be applied to the converted pixels. Alternatively, we calculated a set of new tasseled cap coefficients (Table 6) from the adjusted rescaling factors that can be used directly with the new MSS data (Appendix). Tasseled cap transformations also include TC yellowness, which is not utilized in this study, but its coefficients are included for future reference. We used these new coefficients to calculate TCB, TCG, and TC angle (TCA, see Section 2.4.3) for MSS data in this study.

2.4.3. Cross-sensor, scene-level radiometric normalization

To minimize annual variations in atmospheric conditions, we normalized each image in the Landsat time series to a single reference image. As reference we selected a cloud-free TM image acquired in 1997 (Table 4) and converted it to surface reflectance by means of the COST correction method of Chavez (1996). Following Schroeder et al. (2006), all other TM and ETM+ images in the time series were radiometrically normalized to the COST image using the multivariate alteration detection and calibration algorithm (MADCAL) of Canty et al. (2004). MADCAL identifies invariant pixels between image pairs and performs a relative normalization using orthogonal regression. Water, clouds and cloud shadows were masked out following the methodology in Kennedy et al. (2007a,b). All TM/ETM+ images were then transformed to TCB, TCG, and TCW using the coefficients for reflectance data (Crist, 1985). To normalize MSS data with the TM/ETM+ time series we used TCB and TCG with MADCAL instead of the individual spectral bands (Powell et al., 2008). As with all the Landsat data pre-processing, radiometric normalization was performed across the entire scene (WRS2: path 43, row 29).

Structural differences in forest vegetation have been most effectively described with indices that utilize the contrast between short-wave- and near-infrared reflectance such as TCW (Cohen & Goward, 2004). However, MSS sensors lack short-wave infrared bands, and therefore TCW cannot be computed for Landsat data prior to 1982. Alternatively, we used an index called TC angle (TCA) first introduced by Powell et al. (2010) and computed as follows: TCA = arctan(TCG/TCB). TCA describes the gradient of percent vegetation cover within the TCB-TCG spectral plane (Powell et al., 2010, Gómez et al., 2011), and once calculated for our dataset was the only spectral index used to describe change in this study. However, later, we do use the TCB, TCG, and TCW values at the last image date for statistical modeling.

2.4.4. Cross-sensor, pixel-level alignment

Residual TCA offsets between MSS and TM for some pixels in the scene-level normalized time series were evident (Fig. 2a). To correct for these, we analyzed TCA values from the period between 1984 and 1992 where imagery from MSS and TM were available for the same year (Table 4). We computed the mean bias between MSS and TM TCA from year i to N, and applied it to the MSS time-series as follows:

$$\text{Bias} = \frac{1}{N}\sum_{i=1}^{N} \text{MSS}_i - \text{TM}_i \quad (9)$$

$$\text{MSS}'_i = \text{MSS}_i - \text{Bias} \quad (10)$$

where, MSS'_i is the new TCA value for year i. This final calibration step resulted in what we call the pixel-aligned Landsat time series (Fig. 2b). The pixel-aligned imagery can be easily interpreted without sensor-based interruption across the series (Fig. 3). Across all pixels, average RMSE between MSS-TCA and TM-TCA in the overlapping period was 3.1 (SD = 1.2) before and 2.3 (SD = 0.9) after pixel-level alignment.

2.4.5. Landsat-derived disturbance history

We used the pixel-aligned Landsat time-series to characterize disturbance history for all pixels co-located with field plots (one pixel per plot). Our logic followed that of Cohen et al. (2010) and Kennedy et al. (2010), which temporally dissects each pixel's time trajectory into a series of approximately linear segments, each representing some directional change in spectral index response (Fig. 4). Each segment is given a label associated with disturbance or succession (depending on spectral index used and trend direction) and is bounded by a start and end date vertex. For temporal segmentation of each plot trajectory we used the TimeSync software developed by Cohen et al. (2010) for manual interpretation of land cover change using a time series of Landsat image chips and historic airphotos. First, we determined the change year (start vertex) and the label (fire, harvest, insect and pathogens, recovery, maturation, or stable)

Table 5
Post-calibration dynamic ranges and derived gains and offsets for Landsat 2 data prior to 7/16/1975 (Markham & Barker, 1986, $QCALMIN_{BAND1-4}=0$, $QCALMAX_{BAND1-3}=127$, $QCALMAX_{BAND4}=63$) and for MSS data processed with LPGS 11.2.0 (source: header files) (QCALMIN = 1, QCALMAX = 255). Exoatmospheric irradiance (ESUN) values are from Chander et al. (2009). Because LPGS data are cross-calibrated with Landsat MSS 5, ESUN from Landsat 5 were used for Landsat 1–5 (LPGS).

Landsat	Band	LMIN $W/(m^2\ sr\ \mu m)$	LMAX $W/(m^2\ sr\ \mu m)$	GAIN $(W/m^2\ sr\ \mu m)/DN$	OFFSET $W/m^2\ sr\ \mu m$	$ESUN_\lambda$ $W/m^2\ \mu m$
2 (NLAPS)	1	10	210	1.5748	10	1829
	2	7	156	1.1732	7	1539
	3	7	140	1.0472	7	1268
	4	5	138	2.1111	5	886.6
1 (LPGS)	1	0	243.8	0.9598	−0.9598	1824
	2	10	187.4	0.6984	9.3016	1570
	3	−8.9	170.5	0.7063	−9.6063	1249
	4	0	166.5	0.6555	−0.6555	853.4
2 (LPGS)	1	8.6	288.8	1.1031	7.4969	1824
	2	−0.8	184.6	0.7299	−1.5299	1570
	3	−2.6	151.5	0.6067	−3.2067	1249
	4	4.1	131.7	0.5024	3.5976	853.4
3 (LPGS)	1	4.3	284.7	1.1039	3.1961	1824
	2	3	179.6	0.6953	2.3047	1570
	3	3.1	154.3	0.5953	2.5047	1249
	4	1	127	0.4961	0.5039	853.4
4 (LPGS)	1	2.3	260.8	1.0177	1.2823	1824
	2	4.3	194.5	0.7488	3.5512	1570
	3	4.2	136.7	0.5217	3.6783	1249
	4	3.1	137	0.5272	2.5728	853.4
5 (LPGS)	1	3	268	1.0433	1.9567	1824
	2	3	179	0.6929	2.3071	1570
	3	5	148	0.5630	4.4370	1249
	4	3	123	0.4724	2.5276	853.4

associated with the underlying process or forcing factor for each segment. Next, we used the segmentation fitting routines from the LandTrendr algorithm (Kennedy et al., 2010) to derive fitted TCA values for each trajectory. LandTrendr also segments time series, but, as an automated algorithm, is more prone to interpretation errors than is a human using TimeSync. As we were interested in the most accurate segmentation possible for each plot, we used TimeSync for the actual segmentation. However, even pixel-aligned Landsat TCA time series still contain residual inter-annual noise (e.g. phenology, sun-angle, and residual atmospheric effects) that is minimized by fitting regression lines to each segment and adjusting the TCA values within each segment to the fitted lines (Fig. 4). The application of LandTrendr resulted in a series of interconnected linear segments.

From the fitted time-series for each plot (e.g., Fig. 4) we derived seven sets of quantitative metrics describing the temporal patterns of forest disturbance and recovery (Table 7). The *greatest disturbance* set contains metrics associated with the disturbance segment having the greatest amount of spectral change (b in Fig. 4). The TCA value before and after the disturbance is identified by the TCA value at the beginning (vertex B) and end (vertex C) vertex of this segment (b), respectively. Duration of greatest disturbance is the number of years between vertices (C minus B). Magnitude of the greatest disturbance is the TCA value difference between vertices (C minus B). Relative magnitude is the magnitude of greatest disturbance divided by the TCA value prior to disturbance, and rate of change is the absolute magnitude divided by duration of greatest disturbance. The duration-weighted magnitude highlights subtle but long-term disturbances and is calculated as the product of magnitude and duration of the greatest disturbance. Time since start of greatest disturbance is the number of years between the beginning disturbance year (vertex B) and the year of the last vertex (vertex E). Time since the end of the greatest disturbance is the number of years between the ending disturbance year (vertex C) and the last year (vertex E). Agent of disturbance is a categorical variable that distinguishes between fire, insect-pathogen, and harvest disturbances and is interpreted directly during use of TimeSync Cohen et al. (2010).

The *total disturbance*, *total recovery*, *total no change* and *total all* sets summarize the entire historic Landsat record. Total disturbance magnitude and duration are the sums of the magnitudes and durations of all disturbance segments (e.g., Fig. 4, a plus b). Total recovery magnitude and duration sum the magnitudes and durations of all recovery segments (c and d). The rates of change for total disturbance and total recovery are obtained by dividing change magnitude by change duration. Duration-weighted magnitude was calculated from the product of magnitude and duration similar to the greatest disturbance set, but from the total of all disturbance segments. Total no-change duration is the total number of years across stable segments (none for the plot shown in Fig. 4). The disturbance-recovery ratio is the total disturbance divided by the total recovery. The mean square error (MSE) of the trajectory is the sum of the individual MSEs of the fitted segments weighted by their duration.

The *last monotonic trend* set describes the union of the final segment and any preceding it that have the same directional trend. For

Table 6
Tasseled cap coefficients for Landsat 2 data processed prior to 7/16/1975 (Kauth et al., 1979; Thompson & Wehmanen, 1980), and tasseled cap coefficients for Landsat 1–5 MSS processed with LPGS 11.2.0 coefficients in Table 5.

Landsat	Feature	Band 1	Band 2	Band 3	Band 4	Bias
2 (NLAPS)	Brightness	0.3323	0.6032	0.6758	0.2628	0.0000
	Greenness	−0.2832	−0.6601	0.5774	0.3883	0.0000
	Yellowness	−0.8995	0.4283	0.0759	−0.0408	0.0000
1 (LPGS)	Brightness	0.2031	0.3520	0.4627	0.0848	−12.7421
	Greenness	−0.1731	−0.3852	0.3953	0.1253	−9.5016
	Yellowness	−0.5497	0.2499	0.0520	−0.0132	5.9304
2 (LPGS)	Brightness	0.2334	0.3679	0.3975	0.0650	−11.6690
	Greenness	−0.1989	−0.4026	0.3396	0.0960	−0.6579
	Yellowness	−0.6318	0.2612	0.0446	−0.0101	−2.4038
3 (LPGS)	Brightness	0.2336	0.3504	0.3900	0.0642	−7.3048
	Greenness	−0.1991	−0.3835	0.3332	0.0948	0.6085
	Yellowness	−0.6323	0.2488	0.0438	−0.0100	1.9141
4 (LPGS)	Brightness	0.2153	0.3774	0.3418	0.0682	−6.0451
	Greenness	−0.1835	−0.4130	0.2920	0.1007	1.3184
	Yellowness	−0.5829	0.2680	0.0384	−0.0106	3.5011
5 (LPGS)	Brightness	0.2208	0.3492	0.3688	0.0611	−6.0382
	Greenness	−0.1881	−0.3822	0.3151	0.0903	2.2989
	Yellowness	−0.5976	0.2480	0.0414	−0.0095	2.7263

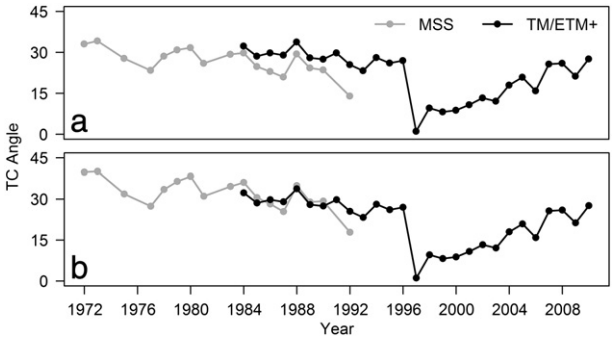

Fig. 2. Example trajectory of a single Landsat pixel showing TCA offset before (a) and after (b) pixel-level alignment of time series. The abrupt decrease of TCA in 1997 was caused by a stand replacing wildfire in August 1996. The disturbance is followed by a slow increase in TCA indicating forest recovery.

the example in Fig. 4, magnitude is TCA of E minus that of C. Likewise, duration is number of years between C and E. Rate of change is magnitude divided by duration, and similar to earlier MSE is also derived for the recent trend.

The final set of metrics describes the *current condition* in terms of TCB, TCG, TCW, and TCA. The tasseled cap indices, when used in unison, capture the three basic dimensions of Landsat spectral space and are generally aligned with gradients of forest cover, composition, and structure Cohen et al. (2010). Landsat metrics were computed in IDL (Interactive Data Language, ITT Visual Information Solutions, Inc.).

2.5. Regression analyses

We performed multiple linear regression analyses to explore the relationships between each forest structure variable (response) and remote sensing variables (predictors). Predictor variables were divided into three main groups: 1) lidar (Table 3), 2) Landsat time series (Table 7 — all variables), and 3) single-date Landsat variables (Table 7 — TC of current condition). Analyses were conducted for each group separately. Prior to building regression models, we removed variables with nearly identical information and thus a high correlation coefficient with other predictor variables ($r > 0.9$). This step did not eliminate colinearity among all variables. However, a lower correlation threshold would have significantly reduced the number of potential lidar predictors, which often tend to be correlated (Muss et al., 2011). To avoid problems associated with over-fitting and colinearity we employed all-subsets regression using the leaps package (Lumley, 2009) in the R statistical language (R Development Core Team, 2011). All-subsets regression does not limit model selection to a single 'best' model, but it performs an exhaustive search for the best subsets of predictor variables. Once the best subsets were identified, we selected the most parsimonious models with the lowest Cp value (Mallows, 1973) approximately equal to the number of parameters and removed models that showed signs of colinearity (variance inflation factors < 5). Cp compares the residual sum of squares for a subset model to the MSE of the full model and is closely related to the adjusted R^2 (R^2_a). For final models we report multiple R^2 and R^2_a. Further, we measured the relative importance of variables using the Lindeman–Merenda–Gold (R^2_{lmg}) metric from the relaimpo package in R (Grömping, 2006). R^2_{lmg} computes

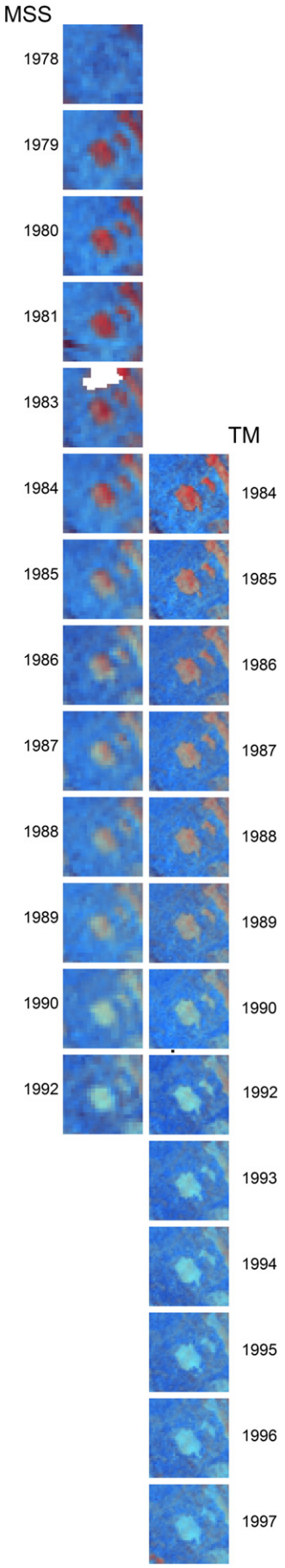

Fig. 3. Image chips of a field plot (center pixel) and its local neighborhood. Tasseled cap brightness, greenness, and angle are displayed as red, green, and blue. The clearcut patches (red) appearing in 1979 begin the process of recovery towards moderately dense cover of young conifer trees (orange to cyan to light blue), which is nearly complete by 1997. Both MSS and TM are shown in the overlap period (1984–1990) and only images between 1978 and 1997 are displayed for illustrative purposes. In practice, once the pixel-level normalization is completed the MSS of the overlap period are discarded. White areas represent cloud-covered pixels that were removed from the dataset.

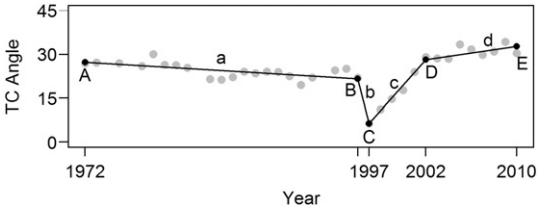

Fig. 4. Example of a normalized Landsat time series for a single pixel, showing yearly tasseled cap angle values (gray dots), the fitted time series (black lines), and the fitted segment start and end vertices (black dots). Downward trending segments represent disturbance (or maturation) and upward trending segments represent recovery. Flat segments (not shown) represent stable segments. A variety of disturbance and succession process (and related) parameters are derived from the fitted segment vertices. For example, the duration for insect disturbance segment a is determined by subtracting the year of vertex A from that of vertex B. The magnitude of change for fire disturbance segment b is calculated from the difference between the TCA values of B and C. The spectral value at vertex C represents the spectral value at the end vertex for the disturbance having the greatest observed magnitude. Time since the end of the greatest disturbance is calculated by subtracting the year of vertex C from that of vertex E for recovery segments c and d.

the average contribution of each variable to the overall R^2 across all possible orderings and thus provides a unique decomposition of the explained variance when predictors are correlated. The interpretation of the method is convenient because individual R^2_{lmg} sum to the multiple R^2 of the model. Finally, we evaluated model performance using leave one out cross-validation, which provides a nearly unbiased estimator of prediction error (Efron & Gong, 1983). For each final model, we computed RMSE of model predictions (from cross-validation) versus observed (field) data.

Final, models and predictor variables were tested for significance ($p<0.05$). Predictor variables were continuous metrics except for agent of greatest disturbance (GDAGT), which was recorded as a categorical variable with four factor levels (fire, insect-pathogen, harvest, and undisturbed). We included GDAGT in the regression models by recoding the four levels using three indicator variables: $GDAGT_{Fire}$, $GDAGT_{Insect}$, and $GDAGT_{Harvest}$ ($GDAGT_{Undisturbed}$ was implicit if the other three were zero).

3. Results

3.1. Prediction models

3.1.1. Lidar estimates of forest structure

3.1.1.1. Live biomass. Individual lidar variables were strongly correlated with live biomass but weakly correlated with dead biomass (Table 3.) Height metrics showed the strongest relationships with live structure: volume fraction (HVOL) with live biomass and basal area, and median and mean height with Lorey mean height. Further, an increase in live biomass was associated with an increase in the intensity variance (ISD). The correlation with dead woody biomass and dead basal area was generally low (e.g. $r<0.2$). Most variables were not statistically significant, except for mean intensity of the top height stratum (IMEAN75), which decreased with dead biomass density, and the standard deviation of vegetation height (HSD), which showed a slight increase with dead biomass density. Six lidar predictor variables showed correlation coefficients greater than 0.9 with other lidar variables and were excluded from the analysis (correlated variables that were kept are shown in parentheses): HMAX (H95PCT), HMEAN (HMEDIAN), H25PCT (HMEDIAN), H75PCT (HMEDIAN), IKURT (ISD), I25PCT (RPC1), and I50PCT (IMEAN).

Most of the variation in live biomass was explained by a single variable: HVOL ($R^2=0.88$, Fig. 5a). Adding other predictor variables did not improve model predictability significantly. When HVOL was excluded from analysis, median height (HMEDIAN, $R^2_{lmg}=0.28$) and canopy cover (CANCOV, $R^2_{lmg}=0.26$) together explained the majority of the variance (78%) in the best subset, which is not surprising as HVOL is the product of CANCOV and HMEAN. Including ISD, a measure of intensity variability, in the alternative model improved the model's R^2 by 4%.

3.1.1.2. Dead biomass. For dead biomass, two best-subsets models were selected with similar performance and model size. The best model explained 22% of the variance in dead biomass and included measures of intensity (IMEAN75, $R^2_{lmg}=0.19$) and height (H95PCT, $R^2_{lmg}=0.03$) associated with the top canopy. However, H95PCT was not significant ($p=0.181$). Therefore, we selected the alternative model ($R^2=0.21$), which did not include intensity, but a measure of height variability (HSD, $R^2_{lmg}=0.16$) and median height (HMEDIAN, $R^2_{lmg}=0.05$) (Fig. 5d).

3.1.1.3. Basal area. Three variables were selected in the best subset for predicting live basal area. Similar to the results for live biomass, HVOL was again the most important variable ($R^2_{lmg}=0.59$). In addition, two variables describing the variation in the top height stratum (HCV75, $R^2_{lmg}=0.17$) and the relative frequency of low vegetation returns (H05PCT, $R^2_{lmg}=0.15$) were selected, respectively. Overall, the model explained 91% of the variance in live basal area (Fig. 5g). In comparison, lidar failed to predict basal area of dead trees ($R^2=0.1$, Fig. 5j). IMEAN75 and HSD were the only variables showing a weak but statistically significant relationship.

3.1.1.4. Stand height. Lorey's mean height was the most accurately estimated structure variable using lidar metrics ($R^2_a=0.96$). The best subset from all-subsets regression contained five variables including HMEDIAN ($R^2_{lmg}=0.35$), H95PCT ($R^2_{lmg}=0.29$), HCV75 ($R^2_{lmg}=0.18$), I95PCT ($R^2_{lmg}=0.07$) and IMEAN75PCT ($R^2_{lmg}=0.07$). The model predicted Lorey height with an RMSE of 1.6 m (Fig. 5m). The best single predictors were HMEDIAN, HVOL, H95PCT, and ISD.

Table 7
Parameters describing Landsat disturbance history.

Scope	Description	Parameter
Greatest disturbance (GD)	TC angle before	$GDTCA_B$
	TC angle after	$GDTCA_A$
	Duration	GDDUR
	Magnitude	GDMAG
	Relative magnitude (GDMAG/$GDTCA_B$)	GDRCH
	Rate (GDMAG/GDDUR)	GDROC
	Weighted Magnitude (GDMAG*GDDUR)	GDMXD
	Time since disturbance start	$GDTSD_S$
	Time since disturbance end (GDTSD − GDDUR)	$GDTSD_E$
Total disturbance (TD)	Magnitude	TDMAG
	Duration	TDDUR
	Rate (TDMAG/TDDUR)	TDROC
	Weighted Magnitude (TDMAG*TDDUR)	TDMXD
Total recovery (TR)	Magnitude	TRMAG
	Duration	TRDUR
	Rate (TRMAG/TRDUR)	TRROC
Total no change (TS)	Duration	TSDUR
Total all (TA)	Disturbance-recovery ratio (TDMAG/TRMAG)	TADRR
	Weighted MSE of fit	TAMSE
Last monotonic trend (LM)	Magnitude	LMMAG
	Duration	LMDUR
	Rate of change (LMMAG/LMDUR)	LMROC
	MSE of fit	LMMSE
Current condition	TC Brightness of 2008 image	LTCB
	TC Greenness of 2008 image	LTCG
	TC Wetness of 2008 image	LTCW
	TC Angle of 2008 image	LTCA

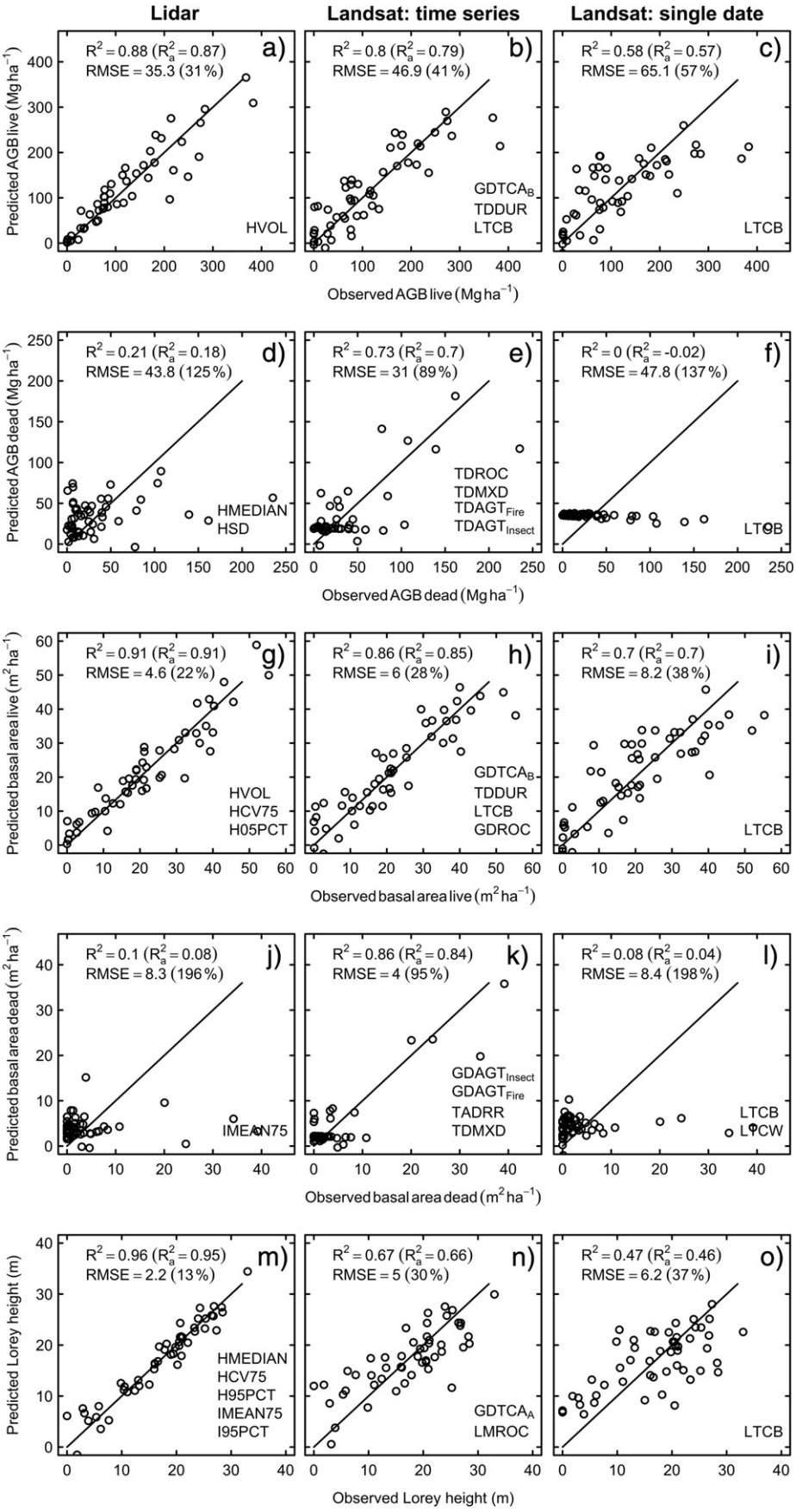

Fig. 5. Predicted (from cross-validation) versus observed forest structure attributes from lidar (left), Landsat time-series (center), and single-date Landsat data (right). Shown are the best models for live biomass (a–c), dead biomass (d–f), basal area of live trees (g–i), basal area of dead trees (j–l), and Lorey height (m–o). The scatterplots show the 1:1 line, adjusted R^2 (R_a), RMSE, and the names of the predictor variables (see Table 7).

Table 8
Correlations between forest structure attributes and disturbance history parameters derived from Landsat (Table 7). Magnitude is negative for disturbances and positive for recovery. As a result, magnitudes of disturbances are negatively correlated with dead biomass and basal area. Shading illustrates the strength of the correlation independent of the sign: from 0 (white) to −1 and 1 (gray). For aboveground biomass (AGB), correlations within individual greatest disturbance agent (GDAGT) classes are shown; however, for basal area (BA) only the correlations across GDAGT are shown.

Parameter	Correlation coefficients								
	AGB live	AGB dead					BA live	BA dead	Height
	All plots	All plots	Fire	Insect	Harvest	Undisturbed	All plots	All plots	All plots
$GDTCA_B$	0.57	0.38	0.88	0.40	-0.29	-	0.48	0.36	0.44
$GDTCA_A$	0.83	-0.08	-0.46	0.26	-0.32	0.35	0.85	-0.04	0.79
GDDUR	0.40	-0.19	-0.11	0.37	0.01	-	0.48	-0.13	0.34
GDMAG	0.38	-0.48	-0.71	-0.34	-0.06	-	0.48	-0.41	0.45
GDRCH	0.45	-0.4 1	-0.59	-0.24	-0.26	-	0.55	-0.33	0.52
GDROC	0.52	-0.36	-0.72	0.15	-0.11	-	0.62	-0.29	0.54
GDMXD	-0.30	-0.49	-0.54	-0.54	-0.03	-	-0.26	-0.46	-0.20
$GDTSD_S$	0.50	-0.19	-0.23	-0.05	-0.12	-	0.56	-0.15	0.43
$GDTSD_E$	0.32	-0.36	-0.22	-0.17	-0.13	-	0.37	-0.29	0.28
TDMAG	0.42	-0.40	-0.55	-0.26	-0.09	-	0.51	-0.37	0.48
TDDUR	0.43	-0.12	-0.36	0.73	0.43	-	0.50	-0.02	0.36
TDROC	0.51	-0.35	-0.89	0.32	0.18	-	0.61	-0.25	0.49
TDMXD	-0.21	-0.52	0.02	-0.82	-0.38	-	-0.18	-0.64	-0.10
$TRMA_G$	-0.46	0.03	-0.05	-0.49	0.10	0.03	-0.47	-0.06	-0.44
TRDUR	-0.01	-0.16	-0.63	-0.34	-0.54	0.34	0.04	-0.19	0.16
TRROC	-0.36	0.18	0.25	-0.47	0.52	0.03	-0.37	0.01	-0.37
TSDUR	-0.04	0.02	0.45	-0.57	-0.12	0.27	-0.03	0.02	-0.04
TADRR	-0.03	-0.33	-0.84	-0.21	-0.02	-	0.01	-0.19	-0.10
TAMSE	0.34	0.19	0.57	0.40	0.00	0.20	0.27	0.20	0.12
LMMAG	-0.31	-0.01	0.20	-0.70	0.04	0.12	-0.33	-0.09	-0.38
LMDUR	0.43	-0.20	0.16	0.42	-0.26	0.00	0.47	-0.06	0.34
LMROC	-0.36	0.11	0.08	-0.49	0.07	0.12	-0.42	0.08	-0.53
LMMSE	0.24	0.07	0.41	0.71	-0.42	0.20	0.19	0.14	0.07
LTCB	-0.76	-0.03	0.14	-0.36	0.01	-0.47	-0.84	-0.08	-0.69
LTCG	-0.11	-0.07	-0.27	-0.30	0.06	0.15	-0.14	-0.21	-0.01
LTCW	0.70	-0.04	-0.28	-0.02	0.00	0.41	0.76	-0.07	0.67
LTCA	0.47	0.03	-0.12	-0.30	0.09	0.33	0.48	-0.06	0.42

3.1.2. Landsat time-series estimates of forest structure

3.1.2.1. Live biomass. Several time-series predictors were correlated with live biomass (Table 8). There were strong correlations between live biomass and TCA after the greatest disturbance ($GDTCA_A$) and TCA before the greatest disturbance ($GDTCA_B$). Correlations between biomass and metrics describing the time and trend of historical events were weaker but also significant. For example, higher biomass densities were associated with lower disturbance rates (GDROC) and longer times since the greatest disturbance ($GDTSD_S$). Relative change (GDRCH) and absolute magnitude (GDMAG) of greatest disturbance showed weaker correlations. For undisturbed plots, MSE of the time-series fit (TAMSE) showed an increase with increased biomass.

All-subsets regression models explained 80% of the variance and included current, single-date TCB (LTCB, $R^2_{Img} = 0.35$, also included in single-date Landsat models), TCA before the greatest disturbance ($GDTCA_B$, $R^2_{Img} = 0.29$), and total disturbance duration (TDDUR, $R^2_{Img} = 0.16$) (Fig. 5b). An alternative model explained 77% of the variance and included $GDTCA_A$ ($R^2_{Img} = 0.39$), LTCB ($R^2_{Img} = 0.28$), and GDROC ($R^2_{Img} = 0.1$). Including information on disturbance agent (GDAGT) did not improve model predictions.

3.1.2.2. Dead biomass. Dead biomass was associated with disturbances and recovery trends, but the effects depended strongly on type of disturbance agent (GDAGT) (Table 8). The weighted magnitudes of the greatest (GDMXD) and total disturbance (TDMXD) were the most informative variables overall. The best subset model across all GDAGT classes included TDMXD ($R^2_{Img} = 0.23$), GDMAG ($R^2_{Img} = 0.18$), and the total MSE of fit for the overall trend (TAMSE, $R^2_{Img} = 0.06$). The model explained 46% of the variance in dead biomass (RMSE = 38.3, $R^2_a = 0.43$). An alternative model that included GDAGT ($R^2_{Img} = 0.24$) and GDMAG ($R^2_{Img} = 0.22$) did not improve model predictions (RMSE = 40.1, $R^2_a = 0.41$). However, examination of the correlation structure suggested a non-additive effect between GDAGT and other predictor variables. For example, dead biomass at fire-disturbed plots ($GDAGT_{Fire}$) was associated with metrics characterizing the intensity of the disturbance, among which $TDROC_{Fire}$ (Fig. 6), $TADRR_{Fire}$, $GDROC_{Fire}$, and $GDMAG_{Fire}$ showed the strongest correlations. Conversely, plots disturbed by insects and pathogens showed relatively weak correlations with these intensity metrics (e.g. $TDROC_{Insect}$), but were more strongly correlated with variables incorporating disturbance duration information. For example, insect-disturbed plots showed high correlations between dead biomass and the weighted magnitude of total disturbance ($TDMXD_{Insect}$, Fig. 6) and total disturbance duration ($TDDUR_{Insect}$); metrics that were only weakly correlated for plots that underwent more rapid disturbance from fire. Interestingly, the rate of change across all (total) disturbances was more strongly correlated with dead biomass from burned plots ($TDROC_{Fire}$) than the rate of change associated with the greatest disturbance only ($GDROC_{Fire}$), suggesting an effect of disturbances preceding fire (e.g. insect). Dead biomass for fire-disturbed plots was also associated with $GDTCA_{B/Fire}$ suggesting a relationship between pre-disturbance forest cover and current dead biomass. In contrast, insect-disturbed plots showed a stronger relationship with the most recent trend ($LMMAG_{Insect}$, $LMMSE_{Insect}$).

Harvested and undisturbed plots had an overall weak relationship but also contained significantly less dead biomass (Table 1).

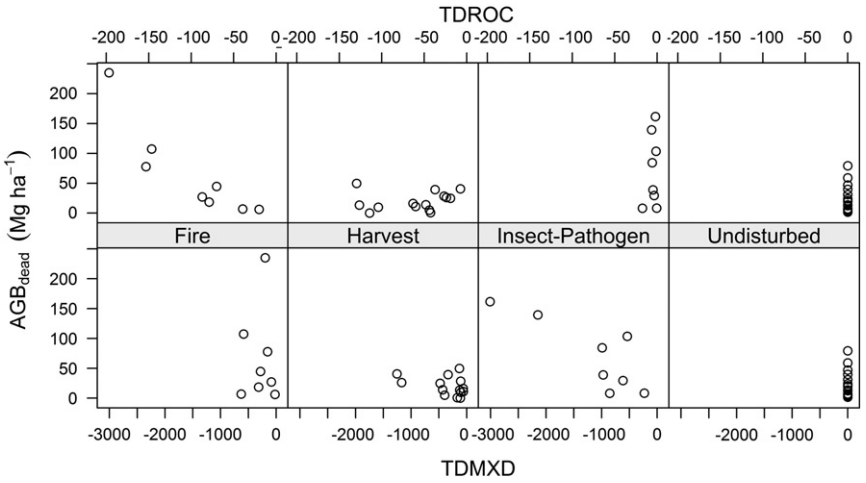

Fig. 6. Aboveground dead biomass (standing plus down wood) versus rate of change of total disturbance (TDROC), and total magnitude weighted by total disturbance duration (TDMXD) for field plots disturbed by fire, harvest, insects and pathogens, and undisturbed plots between 1972 and 2010.

Mean biomass of dead wood at harvested plots was 19.9 Mg ha^{-1} (standard deviation: SD = 15.4) similar to undisturbed plots (mean = 19.4, SD = 20.9 Mg ha^{-1}). In comparison, mean biomass observed at fire- and insect-disturbed plots was approximately three times higher (65.4 Mg ha^{-1} and 71.7 Mg ha, respectively).

To account for differences in the effects of time-series predictors associated with fire and insect disturbances, we built a linear model that included TDROC and TDMXD with interaction terms for fire-disturbance (GDAGT$_{Fire}$) and insect-disturbance (GDAGT$_{Insect}$), respectively:

$$AGB_{dead} \sim DGAGT_{Fire} \times TDROC + DGAGT_{Insect} \times TDMXD. \quad (10)$$

The resulting model explained 73% of the variance and significantly improved predictions of dead biomass (RMSE = 31.0, $R^2_a = 0.7$) (Fig. 5e). The interaction terms were statistically significant ($p<0.05$). Including additional terms to describe the variation in undisturbed and harvested plots was not significant ($p>0.05$).

3.1.2.3. Basal area. Models for live basal area using time-series predictors performed comparably to lidar-based models. The best subset model explained 86% of the variance and predicted live basal area with an RMSE of 6.0 m^2 ha^{-1}. The most important predictors were LTCB ($R^2_{Img} = 0.35$) and GDTCA$_B$ ($R^2_{Img} = 0.21$), and metrics describing the disturbance rate (GDROC, $R^2_{Img} = 0.17$) and duration (TDDUR, $R^2_{Img} = 0.13$) (Fig. 5h). The best subset model for predicting basal area of dead trees had an R^2 of 0.63 and included TDMXD ($R^2_{Img} = 0.33$), GDAGT ($R^2_{Img} = 0.17$), and GDMAG ($R^2_{Img} = 0.13$) ($R^2_{Img} = 0.63$). For fire-disturbed plots, dead basal area was correlated with total disturbance rate (similar to dead biomass) (TDROC$_{Fire}$) but even stronger with total disturbance-recovery ratio (TADRR$_{Fire}$). Similarly, TDMXD$_{Insect}$ was strongly correlated with dead basal area for insect-disturbed plots, as were TDDUR$_{Insect}$ and LMMSE$_{Insect}$. No significant relationship was found for undisturbed plots and harvested plots. Following our logic for estimating dead biomass, we built a final model using indicator variables and interaction terms for TADRR$_{Fire}$ and TDMXD$_{Insect}$. The resulting model explained 86% of the variance with an RMSE of 4.0 m^2 ha^{-1} (Fig. 5k).

3.1.2.4. Stand height. The best subset for predicting Lorey's mean height included GDTCA$_A$ ($R^2_{Img} = 0.51$) and the rate of change of the last monotonic trend (LMROC, $R^2_{Img} = 0.16$). The R^2 of the model was 0.67 with an RMSE of 5.0 m (30% of mean). Other subsets included a larger number of variables (4–5) without improving prediction accuracy. For example, an alternative model was based on LTCB ($R^2_{Img} = 0.39$), LMMAG ($R^2_{Img} = 0.11$), TRROC ($R^2_{Img} = 0.09$), and LTCG ($R^2_{Img} = 0.08$) ($R^2 = 0.64$, RMSE = 5.6 m).

3.1.3. Single-date Landsat estimates of forest structure

Models using current, single-date Landsat data based on TCB (LTCB), TCG (LTCG), TCW (LTCW), and TCA (LTCA) were inferior to models using lidar or Landsat time-series predictors. Correlations with field data were strongest for LTCB, whereas LTCG was not statistically significant ($p>0.05$). Models based on LTCB alone explained 70% of the variance in live basal area (Fig. 5i), 58% of the variance in live biomass (Fig. 5c), and 47% in Lorey's mean height (Fig. 5o). Including LTCW and LTCA did not improve model performance. However, LTCW was correlated with LTCB ($r = -0.86$), and LTCA was

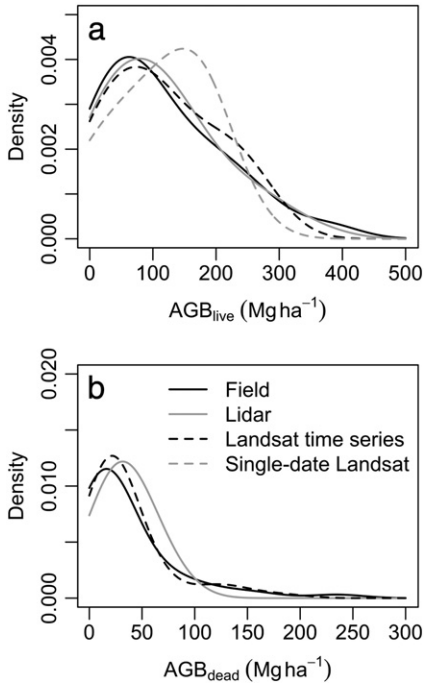

Fig. 7. Density distributions of live (a) and dead (b) biomass predicted (from cross-validation) by models using lidar, Landsat time-series (derived from TimeSync observations and fitted LandTrendr vertices), and single-date Landsat data in comparison to field estimates. No adequate model was found for predicting dead biomass with single-date Landsat data.

correlated with LTCW (r = 0.83). We did not find an adequate model for dead woody biomass and basal area of dead trees using single-date Landsat data (Fig. 5f and l).

3.1.4. Probability density functions of live and dead biomass

Distributional differences between field-measured and predicted AGB can be examined using kernel density functions (Fig. 7). For AGB_{live}, distributions from lidar and Landsat time-series predictions exhibited only minor differences relative to the field measurements, whereas distributions from single-date Landsat models were strikingly different (Fig. 7a). All three datasets predicted the field-observed live biomass of 113 Mg ha^{-1} with minimal bias, but the difference between median predicted biomass and field-measured biomass was significantly higher for single-date Landsat predictions (33.4 Mg ha^{-1}, 38% of the median) than for lidar (12.9 Mg ha^{-1}, 15%), and Landsat time-series models (14.6 Mg ha^{-1}, 17%). Single-date models significantly overestimated low biomass stands (50–100 Mg ha^{-1}) but then saturated (approximated by the mode) between 150 and 200 Mg ha^{-1}. In comparison, models from time-series data extended the dynamic range of biomass (approximated by the smaller second mode) to 250–300 Mg ha^{-1}. Overall, models using time-series predictors preserved the variance in the field measurements (standard deviation of the predicted data divided by the standard deviation of the observed data, $SD_{ratio} = 0.89$) better than models from single-date data ($SD_{ratio} = 0.76$), and were comparable to lidar-based models ($SD_{ratio} = 0.93$).

For dead biomass (Fig. 7b), lidar estimates deviated significantly from the field median (bias = 14.6 Mg ha^{-1}, 79%, and bias = 16.6 Mg ha^{-1}, 90%, respectively). Lidar significantly overestimated low biomass densities of dead wood while significantly underestimating higher biomass density (<50 Mg ha^{-1}). In comparison, Landsat time-series estimates were close to the median field biomass (bias = 1.6 Mg ha^{-1}, 8.4%). Time-series models preserved the variance in the field estimates ($SD_{ratio} = 0.84$) better than lidar models ($SD_{ratio} = 0.46$). Single-date Landsat models did not explain any variation in dead biomass.

4. Discussion

4.1. The role of Landsat time series and lidar for predicting forest structure

This study explored the potential of using Landsat-derived disturbance history parameters to estimate forest biophysical structure in comparison to single-date Landsat data and discrete-return, airborne lidar data. There are well-documented limitations of single-date Landsat data for mapping forest structure (e.g. Lu, 2006), and there is a consensus in the remote sensing community that active remote sensors such as lidar and InSAR (Treuhaft et al., 2004) are more accurate and therefore more suitable for many applications. But the motivation of this study was not to challenge the capabilities of lidar, rather to search for alternative approaches that could potentially extend the spatial and temporal coverage of lidar observations. With a lack of a suitable vegetation-relevant spaceborne sensor and the great expense of airborne lidar, the availability of lidar will remain limited in the near future. The high costs of airborne lidar further limit the repeatability of data acquisitions whereas Landsat data can provide near annual imagery for large parts of the northern hemisphere. We have demonstrated that Landsat data are considerably more useful for mapping forest structure than has previously been appreciated; but only if time series are used to extract information relevant to detailed forest disturbance history. Landsat data exist globally, although the temporal depth of the archive, especially in cloudy areas, may be limited. However, with the recent opening of the US archive for free access (Woodcock et al., 2008) and ongoing repatriation of foreign retrieving station data, there has never before been such a meaningful opportunity to exploit arguably one of the most valuable global remote sensing datasets.

We compared Landsat-based models with lidar-based models of forest biophysical structure as a best-case reference for what remote sensing can currently provide for live trees. A comparison of our results with other studies would have been difficult because of differences in forest conditions, sampling designs and measurement protocols. In this study, we did not integrate lidar and Landsat to map forest structure. However, there are potential synergies between lidar and Landsat time series, and studies have started to explore these (Wulder et al., 2009). Because the collection of field data is expensive (especially in remote regions), lidar could provide a more rigorous sample (at least for live forest structure) that could help to calibrate and describe Landsat's disturbance and recovery trajectories over a broader range of environmental conditions and disturbance types. There have been a few studies that used lidar samples to train Landsat-based models for predicting forest structure but these used single-date imagery (Armston et al., 2009; Hudak et al., 2002; Wulder & Seemann, 2003). Using lidar samples from ICESat-I and the upcoming ICESat-II may also help in understanding how these concepts are applicable to larger scales. However, like Landsat, ICESat waveforms require calibration with data from field measurements or airborne lidar.

4.2. Using the MSS archive

Including the MSS archive in this study enabled us to extend the Landsat time series by more than a decade back to 1972. We did not test for statistical differences between predicting forest structure with and without MSS data. However, the forest disturbance and recovery trends in this study are complex and long-term processes; several activities from timber harvests and insects would have been missed if the analysis were limited to the TM/ETM+ era (Figs. 8 and 9). The sensitivity of the derived models to the length and density of the time series will need to be tested with a larger training sample potentially derived from the lidar data set. Knowledge of the required time length can be useful not only for predicting forest structure of current time periods, but potentially for estimating historic forest parameters by applying the derived models back trough time. Another advantage of extending time series is only indirectly related to the length of time required to accurately estimate forest structure, but results from the fact that trend-fitting algorithms often exhibit larger errors at the beginning and end of the observation periods (Hostert et al., 2003; Kennedy et al., 2010). Thus, a successful integration of the MSS archive also increases the confidence in the fitting of the early TM time periods.

The use of the MSS imagery presented several challenges. More recently, the MSS archive has been reprocessed for better radiometric and geometric fidelity. As with the TM/ETM+ archive, the majority of the imagery is now available with precision terrain correction, which represents a tremendous improvement. Nevertheless, in our study the geometric accuracy of MSS data was not as high as the TM/ETM+ data, introducing additional sources of error. Studies that tested the effect of misregistration on change detection results (Townshend et al., 1992; Dai & Khorram, 1998) recommend image-registration accuracies at the sub-pixel scale (e.g. RMSE<0.5 pixels). That means that additional geometric correction would be required if MSS data is to be used in pixel-level time-series analysis. We used an automated program to geometrically align all MSS images in the time series, but doing that for large-area applications (e.g., Masek et al., 2008) could be problematic.

To bridge radiometric differences between MSS and TM data we used tasseled cap indices. The transformation is consistent between the two sensors (Crist & Cicone, 1984) and has been shown to describe vegetation patterns consistently across broad geographic ranges (Lobser & Cohen, 2007). Unlike for TM and ETM+, however, there are no reflectance-based coefficients for MSS. Using post-

calibration coefficients available at the time, we corrected for differences in the post-calibration dynamic ranges of MSS data. The MSS tasseled cap coefficients we derived (Table 6) are valid as long as the post-calibration coefficients for MSS (Table 5) do not change. Users should check the metadata information supplied with the Landsat data. As a DN-based transformation, MSS tasseled cap is influenced by temporal variations in atmospheric constituents. We minimized this source of error by means of relative normalization (Canty et al., 2004) of all images in the time series to an atmospherically corrected reference. Relative normalization ensures a strong level of temporal consistency (Schroeder et al., 2007) and is often applied in time-series studies (Powell et al., 2008; Powell et al., 2010; Kennedy et al., 2007a,b; Kennedy et al., 2010; Gómez et al., 2011). Residual biases between MSS and TM time-series were small and adjusted for using a pixel-level alignment. Finally, we used a trajectory-fitting algorithm (Kennedy et al., 2010) to minimize inter-annual noise caused by residual atmospheric effects and sun-angle differences.

To describe inter-annual changes and trends in forest disturbance and recovery we used a single spectral index. TCA has been previously shown to capture forest cover changes adequately (Powell et al., 2010; Gómez et al., 2011). In this study, single-date TCA associated with the current condition showed a weaker direct correlation with forest structure than single-date TCB. We chose TCA, because our experience and early testing revealed a general superiority of TCA over TCB and TCG for identifying percent cover change (time-series segmentation). However, it is possible to use different indices for segmentation (identify time of events) and trajectory fitting (identify spectral values of events), which might improve estimates of forest structure. One could also use the Normalized Difference Vegetation Index (NDVI), which should be highly correlated with TCA. However, NDVI is a single index derived from multivariate spectral space, whereas the tasseled cap is a multidimensional index set derived from the same multivariate data-space (Jackson, 1983), so there is a potential advantage to using the tasseled cap transformation (Cohen & Goward, 2004). Additionally, TCA has a companion index: TCD (tasseled cap distance, Duane et al., 2010), which is sensitive to cover quality rather than cover percent. As such, TCD distinguishes between younger and older conifer forests (Duane et al., 2010), and as observed in other related work, cover type (e.g., conifer, hardwood, grass). Consequently, used in combination, TCA and TCD are potentially more powerful than either alone. TCA and TCD are actually not new concepts, as they were originally derived for change vector analysis (Malila, 1980), and simply transform the Cartesian coordinate system of the tasseled cap to a polar coordinate system, or for TM/ETM+ data to a spherical system (Allen & Kupfer, 2000).

4.3. Predicting forest structure of live trees

From this study, the superior performance of lidar to estimate live forest structure is not surprising and is supported by numerous studies (e.g. Lefsky et al., 2002; Hudak et al., 2006). Interestingly, AGB_{live} models were best explained by a simple metric only: HVOL, which is related to the lidar observed volume occupied by vegetation surfaces (Kim et al., 2009). Average prediction error was smaller for young stands and increased with higher biomass densities ($Mg\ ha^{-1} > 100$). Because HVOL is relative to the mean lidar height, a possible explanation is that the sensitivity of HVOL decreased with increasing vertical complexity; the height distribution in young conifer stands was relatively homogenous compared to older conifer stands that tended to be more open and vertically differentiated. Lidar models of live basal area and Lorey's height performed better than the live biomass model, but included multiple predictor variables. Our results are based on a comprehensive set of metrics, most of which have been tested in other studies (e.g. Hudak et al., 2008; Kim et al., 2009). We defined lidar here as the 'best possible' scenario, but it is still an evolving technology and not a fixed standard. However, lidar is subject to availability, and is extremely limited across most of the Earth's surface.

This study found significant relationships between current forest structure from field measurements and disturbance history derived from 38 years of annual Landsat imagery. Exploiting these relationships significantly improved prediction of live forest biomass, basal area, and stand height, compared to models using Landsat data acquired for a single year. Estimates of live biomass from single-date Landsat data showed a saturation effect between 150 and 200 $Mg\ ha^{-1}$ with an average prediction error of 65.1 $Mg\ ha^{-1}$ (RMSE). Including temporal information on disturbance and recovery trends considerably improved AGB_{live} estimates (RMSE = 46.9 $Mg\ ha^{-1}$) and increased the sensitivity by at least 100 $Mg\ ha^{-1}$ to 250–350 $Mg\ ha^{-1}$. As a result, prediction accuracy was much closer to that obtained from lidar metrics (RMSE = 35.3 $Mg\ ha^{-1}$). This was equally true for live basal area and Lorey's height. Perhaps most important, however, was that frequency distributions of predictions from lidar and Landsat time series were nearly identical, which has important mapping implications, especially when maps of forest structure are used in non-linear ecosystem models (Duane et al., 2010).

4.4. Predicting dead woody biomass and basal area

In contrast to models of live forest structure variables, time-series models yielded significantly better estimates of dead biomass and dead basal area than did lidar models. Some studies have had moderate success using lidar to estimate standing dead biomass (Bater et al., 2009; Kim et al., 2009; Pesonen et al., 2008). Kim et al. (2009), for example, estimated standing dead biomass at a site in Northern Arizona ($R^2 = 0.62$, RMSE = 41.5 $Mg\ ha^{-1}$, 63% of mean versus RMSE = 43.8 $Mg\ ha^{-1}$, 125% in this study), revealing important differences between stands that were burned and stands that were not burned in large wildfires. Kim et al. (2009) used the relative frequency peak of low intensity returns of the lidar data to build regression models, and suggested that a height stratification of lidar intensity could improve results, but did not test this. In this study, we tested a height-stratified intensity metric using the 75th height percentile to capture the intensity of the lidar reflections from the top canopy (IMEAN75). We found that lidar intensity of the top canopy decreased with increased levels of dead biomass, whereas other lidar intensity metrics did not show a significant relationship (Table 3). One reason for the weak relationship here could be that our dead woody biomass included down logs, which cannot easily be observed with lidar data. However, with the approach used in this study, the correlation did not improve when only standing dead trees were analyzed. Pesonen et al. (2008) used height and intensity metrics to estimate dead wood volume and found a better prediction accuracy for downed dead wood volume (RMSE = 51%) than for standing dead wood volume (RMSE = 78%), despite there being little relationship between field measured live and dead trees. Because lidar intensity is not a calibrated measurement and variable across sensors and flight conditions (Korpela et al., 2010) it is difficult to compare results across studies. However, it is important to note that research on lidar-based estimation of dead biomass is still new and will likely evolve with new technological developments (e.g. waveform and multi-spectral lidar).

The capability to estimate dead standing and down woody biomass with Landsat time series has important practical significance for spatially explicit ecosystem modeling. We found high correlations with time-series predictors and dead woody biomass and basal area, but the relationships varied by disturbance agent. For harvested and undisturbed plots, we found no significant relationships. For harvested areas, this is understandable because woody debris is usually removed from the site and patterns of remaining dead wood are

strongly affected by forest management practices (Kennedy et al., 2008). For example, if the range of activity fuel treatments varied widely in the study area, then dead biomass associated with management would be difficult to predict. Mean and variance of dead biomass at undisturbed plots was similar to that of harvested plots and significantly lower compared to disturbed plots. For applications of these results in a mapping context, a disturbance agent must be characterized for each disturbed patch, which has been a difficult task and is largely not attempted (e.g., Masek et al., 2008; Huang et al., 2010) or is hand-digitized (Cohen et al., 2002; Healey et al., 2008). Mapping the disturbance agent is now an important focus of Landsat-based change detection research (Schroeder et al., 2011; Kennedy et al. 2012); therefore, the finding that dead biomass can be estimated using Landsat time series is timely.

Standing and down woody debris play important roles for biodiversity and carbon sequestration (Harmon et al., 1986), but these parameters have been difficult to obtain with remote sensing, especially with Landsat data. Landsat measures the reflective properties of forest canopies. Thus, the amount of dead woody biomass can only be inferred indirectly when tree mortality is associated with detectable structural and compositional changes in the canopy. Here, we found that dead biomass is indirectly related to the spectral change magnitude and duration of disturbance events. Our findings are based on a relatively small sample; the robustness of these relationships across a larger region remains to be tested.

4.5. Visual interpretation of Landsat's disturbance history

Differentiation between long-term disturbances from insects and short-term disturbances from fire and harvest was important to predict dead biomass. To visualize the interactions between disturbance agent and dead biomass, we provide graphical representations of TCA time series for each plot (Fig. 8). We did not convert TCA to a biophysical unit, but the index corresponds with a gradient in vegetation cover (Powell et al., 2010; Gómez et al., 2011). Within each category, the plots were sorted by dead biomass density. For fire-disturbed plots (most, but not all, fires occurred in August 1996 and were first detected in 1997) current dead biomass is largely a positive function of disturbance magnitude (light orange to red immediately after the fire event), which also is inversely associated with the pre-fire cover gradient (green to light orange). For insect-disturbed plots, the amount of dead biomass is largely a function of duration of disturbance (number of years the TCA trend goes from greener to more orange) but also the number of years of recovery since disturbance (increasing trend towards green). In undisturbed plots, the amount of dead biomass is mostly associated with the amount of cover as

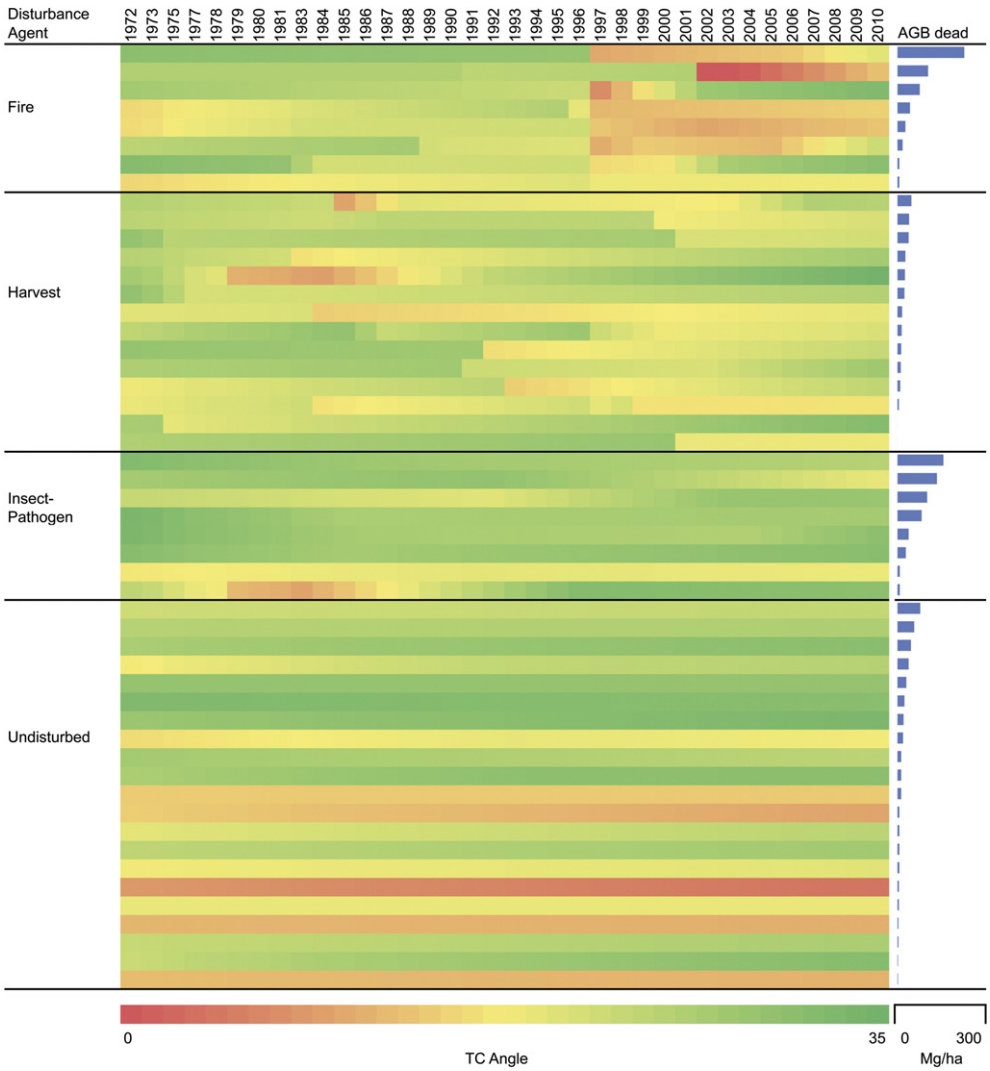

Fig. 8. Fitted time series of tasseled cap angle (TCA) grouped by disturbance agent and sorted by aboveground dead biomass (AGB). TCA increases (low to high: red–yellow–green) with increasing vegetation cover.

indicated by the positive relationship with TCA (red to green). For harvest plots there is no clear pattern with TCA values over time. These interpretations are consistent with our regression analysis results, but provide a different, and perhaps more comprehensive, view of the observed relationships.

Similar graphical representations for live biomass are useful but show weaker patterns (Fig. 9). For burned plots, there is an inverse relationship to that observed for dead biomass, with higher values for stands having lower magnitude disturbances, as should be expected. For insects, the amount of live biomass is a complex interaction of time since end of disturbance, pre disturbance cover, and rate of recovery towards increasing canopy cover. For harvest plots there seems to be no association with current amount of forest cover (as indicated by TCA values at the current time), and no clear indication of temporal patterns. However, there is a somewhat weak, but nonetheless distinctive trend associated with time since disturbance; although the relationship is opposite to that expected, with more recent disturbances having more live biomass. This could be a function of an increasing tendency on federal ownerships in this region towards lighter thinnings, with increasing attention to other ecosystem service besides wood production. But this also highlights a potential short-coming of using TCA for indicating biomass amount, given that TCA is not formulated to discriminate between understory deciduous and overstory coniferous species. For undisturbed plots, there is a clear and distinct progression of higher cover associated with higher live biomass. Moreover, there is a weak but notable trend in TCA over time (towards increasing cover) for most plots that enhances the ability of time series (over that of single date) imagery to predict current biomass. However, we did not stratify live biomass by disturbance agent, as we had done for dead biomass, because it did not improve prediction accuracy.

4.6. Application of the concepts to a larger landscape

This study represented a proof-of-concept that parameters derived from Landsat time-series trajectories are useful for predicting forest structure. The trajectories were obtained through manual interpretation with TimeSync software (Cohen et al., 2010), but the methods can be automated using LandTrendr (Kennedy et al., 2010). Because the sample size was limited by the number of field plots, we chose a manual interpretation method to minimize errors associated with automated algorithms. However, the trajectory fitting used in this study is consistent with the automated LandTrendr algorithm (Kennedy et al., 2010), which for whole Landsat scenes, could replace our use of TimeSync. Required, however, may be a new set of disturbance and recovery metrics – similar to those used here – than the standard set currently produced (Kennedy et al., 2010).

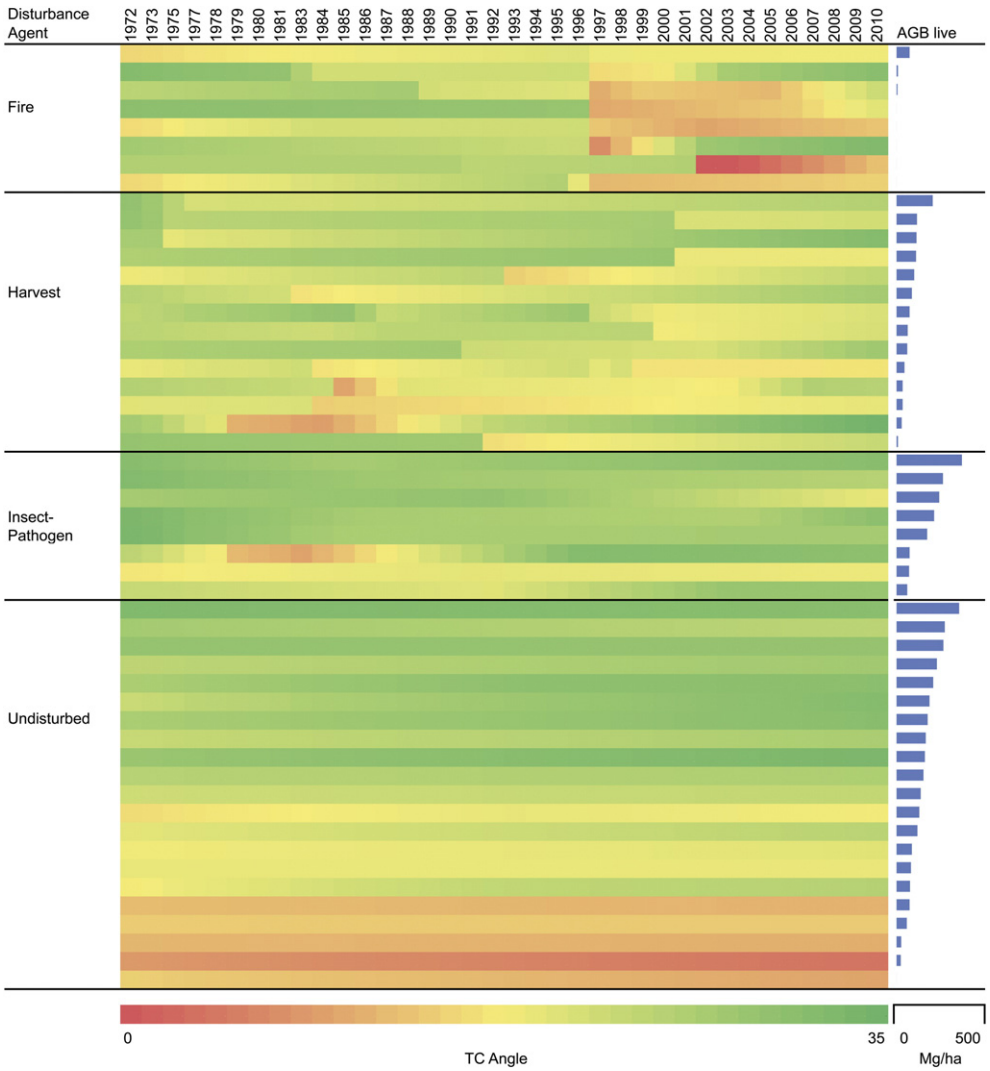

Fig. 9. Fitted time series of tasseled cap angle (TCA) grouped by disturbance agent and sorted by aboveground live biomass. TCA increases (low to high: red–yellow–green) with increasing vegetation cover.

We showed that Landsat-derived disturbance and recovery information was important for predicting current live biomass and mortality in our coniferous forest site in Eastern Oregon. We calculated several sets of metrics from time-series trajectories that we assumed to be relevant for characterizing forest structure in this system, e.g. disturbance magnitude weighted by disturbance duration to differentiated between abrupt–intense disturbances (fire) and long–slow disturbances (insects). We also included MSE metrics, which describe the inter-annual residuals in TCA around the segmentation lines. Because variations in sun-target-sensor viewing geometry increase with the structural complexity of forest canopies (Cohen & Spies, 1992), we hypothesized that MSE metrics increase with forest age, and including them would improve differentiation of older, high biomass stands. However, we found only a weak but statistically significant correlation between the MSE of the most recent trend and live biomass at undisturbed plots. Because of the relatively small number of undisturbed field plots, we did not account for topographic effects (nor did we apply topographic correction to the imagery). However, our study site is characterized by complex topography, which complicates inferences based on MSE metrics. For example, the correlation between MSE metrics and forest parameters could 1) decrease with the effect of topography on inter-annual variations in canopy reflectance and 2) artificially increase when forest attributes are correlated with topography.

Because disturbance metrics are only indirectly related to forest biophysical structure, the geographic region of applicability of the derived relationships to forest sites outside the study area needs to be tested. We believe our general sets of metrics are relevant for other forest sites where disturbance and recovery processes can be observed with satellite imagery over several years (e.g. boreal and other temperate forests). However, the relative importance of the variables may change with the nature of the disturbance regime. Considering that our study area is very complex with respect to topography, forest structure and disturbance history, the applicability of the presented method to other areas is promising.

5. Conclusions

We extracted metrics describing annual trends in forest disturbance and recovery from annual Landsat time series with the objective to predict current forest structure, and compared the results to predictions from lidar and single-date Landsat data. Landsat time-series metrics significantly improved predictions of live aboveground biomass (AGB_{live}), basal area (BA_{live}) and stand height compared to single-date Landsat data. We found a strong relationship between post-disturbance vegetation cover (as expressed by TC Angle) and current forest structure, which highlights the importance of detecting the time of disturbance accurately. Lidar predicted AGB_{live}, BA_{live}, and stand height most accurately, but estimates of AGB_{live} and BA_{live} from Landsat time-series models were remarkably similar. Because the spatial coverage of lidar is limited, Landsat time-series metrics could represent a viable alternative for estimating forest structure attributes in our study region.

Lidar metrics were the best predictors for live tree biomass, but Landsat time-series metrics captured the variation in dead woody biomass significantly better (AGB_{dead}). Most of the AGB_{dead} originated from insect- and fire-induced tree mortality, and information on the disturbance agent was important for accurate predictions. For insect-disturbed plots, AGB_{dead} was associated with disturbance magnitude after accounting for differences in disturbance durations. For fire-disturbed plots, AGB_{dead} was associated with the magnitude of the fire disturbance, but including information on pre- and post-fire trends significantly improved predictions of AGB_{dead}.

The mixed-conifer forests in this study are the results of complex interactions of different disturbance agents. A long history of wildfires, insect outbreaks, and harvest activities has created structurally complex forests. Suppression of fires in the past several decades has resulted in smaller, low-severity fires, which decreased landscape heterogeneity, and increased stand densities and the likelihood of high severity fire events (Schoennagel et al., 2004). The Landsat data archive provides a unique opportunity to study the effects of past disturbance interactions on current forest structure. Taking advantage of the full Landsat data record means that MSS data must be seamlessly integrated with TM and ETM+ imagery, and we have described one approach to accomplish this. Because of the lower spectral resolution and lower signal to noise ratio, MSS sensors have a lower sensitivity to subtle vegetation changes. For long-term trends, using dense time series partly offset this effect by increasing the number of observations. Finally, predicting forest structure in complex disturbance systems requires a long data record, but also change-detection algorithms algorithms that are able to capture both rapid changes and long-term processes. The outlook is promising. In the last few years, Landsat change detection has made significant progress from relatively simple and standard bi-temporal analyses to sophisticated algorithms that explicitly leverage the power of annual Landsat time series (Huang et al., 2010; Kennedy et al., 2010). The continuity of the Landsat data mission in the near future is a critical requirement not only to continue the study of historic changes, but also to understand the linkages between these changes and our current environment. Without availability of free, high quality data, little of this would be possible.

Acknowledgments

This research was supported by NASA Headquarters under the NASA Earth and Space Science Fellowship Program – Grant "NNX10AN49H" and by the Oregon Watershed Enhancement Board. We thank Dr. Zhiqiang Yang for his comments on the MSS tasseled cap calculations, the USGS EROS data center for early access to the MSS archive, Dr. Demetrios Gatziolis for his help with lidar data processing, Aaron Richards, Daniela White, and Candy Mollnau for their field assistance, and Dr. Keith Jayawickrama for providing the field hypsometer. We also thank six anonymous reviewers for their valuable comments.

Appendix

Here we describe in detail the conversion of the original Landsat 2 (reference) tasseled cap coefficients for recent MSS data (input). Consistent with the text (Section 2.4.1), we use subscript R to denote parameters of the reference data, subscript I for parameters of the input data, and subscript A for adjusted coefficients.

The tasseled cap is a linear transformation, which can be written with respect to the reference data as follows:

$$TC^k = \sum_{i=1}^{4} \beta_R{}^{k,i} Q_R^i \tag{11}$$

where,

TC^k	k-th tasseled cap component
$\beta_R^{k,i}$	coefficient of tasseled cap component k for band i
Q_R^i	quantized calibrated pixel value of band i [DN].

Using the adjusted rescaling gain G_A and bias B_A factors (Eqs. 7 and 8), reference pixel values Q_R can be substituted with the input MSS data Q_I as follows:

$$TC^k = \sum_{i=1}^{4} \beta_R^{k,i} G_A^i Q_I^i + \beta_R^{k,i} B_A^i. \tag{12}$$

From Eq. (12), we can obtain a new set of (adjusted) tasseled cap coefficients:

$$\beta_A^{k,i} = \beta_R^{k,i} G_A^i \tag{13}$$

$$\alpha_A^k = \sum_{i=1}^{4} \beta_R^{k,i} B_A^i \tag{14}$$

where,

$\beta_A^{k,i}$ = adjusted coefficient of tasseled cap component k for band i
α_A^k = new additive term for tasseled cap component k

Finally, the tasseled cap transformation can be expressed with respect to the input data using the adjusted coefficients (including the additive term) as follows:

$$TC^k = \alpha_A^k + \sum_{i=1}^{4} \beta_A{}^{k,i} \times Q_i^i. \tag{15}$$

References

Allen, T. R., & Kupfer, J. A. (2000). Application of spherical statistics to change vector analysis of Landsat data: Southern Appalachian spruce-fir forests. *Remote Sensing of Environment*, *74*, 482–493.

Andersen, H. E., McGaughey, R. J., & Reutebuch, S. E. (2005). Estimating forest canopy fuel parameters using LIDAR data. *Remote Sensing of Environment*, *94*, 441–449.

Armston, John D., Denham, Robert J., Danaher, Tim J., Scarth, Peter F., & Moffiet, Trevor N. (2009). Prediction and validation of foliage projective cover from Landsat-5 TM and Landsat-7 ETM+ imagery. *Journal of Applied Remote Sensing*, *Volume 3*(Issue 1).

Baker, J. P., Hulse, D. W., Gregory, S. V., White, D., Van Sickle, J., Berger, P. A., Dole, D., & Schumaker, N. H. (2004). Alternative futures for the Willamette River Basin, Oregon. *Ecological Applications*, *14*, 313–324.

Bater, C. W., Coops, N. C., Gergel, S. E., LeMay, V., & Collins, D. (2009). Estimation of standing dead tree class distributions in northwest coastal forests using lidar remote sensing. *Canadian Journal of Forest Research-Revue Canadienne De Recherche Forestiere*, *39*, 1080–1091.

Bergen, K. M., Goetz, S. J., Dubayah, R. O., Henebry, G. M., Hunsaker, C. T., Imhoff, M. L., Nelson, R. F., Parker, G. G., & Radeloff, V. C. (2009). Remote sensing of vegetation 3-D structure for biodiversity and habitat: review and implications for lidar and radar spaceborne missions. *Journal of Geophysical Research-Biogeosciences*, *114* G00E06: 13p.

Campbell, Sally, Liegel, Leon, & tech. coords. (1996). Disturbance and forest health in Oregon and Washington. Gen. Tech. Rep. PNW-GTR-381. *Pacific Northwest Research Station, Pacific Northwest Region; Oregon Department of Forestry; Washington Department of Natural Resources*. Portland, OR: U.S. Department of Agriculture, Forest Service 105 p..

Canty, M. J., Nielsen, A. A., & Schmidt, M. (2004). Automatic radiometric normalization of multitemporal satellite imagery. *Remote Sensing of Environment*, *91*, 441–451.

Chander, G., Markham, B. L., & Helder, D. L. (2009). Summary of current radiometric calibration coefficients for Landsat MSS, TM, ETM+, and EO-1 ALI sensors. *Remote Sensing of Environment*, *113*, 893–903.

Chavez, P. S. (1996). Imaged-Based Atmospheric Corrections - Revisited and Improved. *Photogrammetric Engineering and Remote Sensing*, *62*, 1025–1036.

Cohen, W. B., & Spies, T. A. (1992). Estimating structural attributes of Douglas-Fir/Western Hemlock forest stands from Landsat and Spot Imagery. *Remote Sensing of Environment*, *41*, 1–17.

Cohen, W. B., Yang, Z., & Kennedy, R. E. (2010). Detecting trends in forest disturbance and recovery using yearly Landsat time series: 2. TimeSync - Tools for calibration and validation. *Remote Sensing of Environment*, *114*, 2911–2924.

Cohen, W. B., Spies, T. A., Alig, R. J., Oetter, D. R., Maiersperger, T. K., & Fiorella, M. (2002). Characterizing 23 Years (1972–95) of stand replacement disturbance in Western Oregon forests with Landsat imagery. *Ecosystems*, *5*, 122–137.

Cohen, W. B., & Goward, S. N. (2004). Landsat's role in ecological applications of remote sensing. *Bioscience*, *54*, 535–545.

Crist, E. P., & Cicone, R. C. (1984). A physically-based transformation of Thematic Mapper data = The TM Tasseled Cap. *IEEE Transactions on Geoscience and Remote Sensing*, *GE-22*, 256–263.

Crist, E. P. (1985). A TM tasseled cap equivalent transformation for reflectance factor data. *Remote Sensing of Environment*, *17*, 301–306.

Dai, X., & Khorram, S. (1998). The effects of image misregistration on the accuracy of remotely sensed change detection. *IEEE Transactions on Geoscience and Remote Sensing*, *36*, 1566–1577.

Drake, J. B., Knox, R. G., Dubayah, R. O., Clark, D. B., Condit, R., Blair, J. B., & Hofton, M. (2003). Above-ground biomass estimation in closed canopy Neotropical forests using lidar remote sensing: Factors affecting the generality of relationships. *Global Ecology and Biogeography*, *12*, 147–159.

Duane, M. V., Cohen, W. B., Campbell, J. L., Hudiburg, T., Turner, D. P., & Weyermann, D. (2010). Implications of alternative field-sampling designs on Landsat-based mapping of stand age and carbon stocks in Oregon forests. *Forest Science*, *56*, 405–416.

Efron, B., & Gong, G. (1983). A leisurely look at the bootstrap, the jackknife, and cross-validation. *The American Statistician*, *37*, 36–48.

Falkowski, M. J., Evans, J. S., Martinuzzi, S., Gessler, P. E., & Hudak, A. T. (2009). Characterizing forest succession with lidar data: An evaluation for the Inland Northwest, USA. *Remote Sensing of Environment*, *113*, 946–956.

Franklin, J. F., & Dyrness, C. T. (1988). *Natural vegetation of Oregon and Washington*. Corvallis, OR: Oregon State Univerity Press.

Goodwin, N. R., Coops, N. C., Wulder, M. A., Gillanders, S., Schroeder, T. A., & Nelson, T. (2008). Estimation of insect infestation dynamics using a temporal sequence of Landsat data. *Remote Sensing of Environment*, *112*, 3680–3689.

Gómez, C., White, J. C., & Wulder, M. A. (2011). Characterizing the state and processes of change in a dynamic forest environment using hierarchical spatio-temporal segmentation. *Remote Sensing of Environment*, *115*, 1665–1679.

Grömping, U. (2006). Relative importance for linear regression in R: The Package relaimpo. *Journal of Statistical Software*, *17*(1), 1–27.

Gough, C. M., Vogel, C. S., Schmid, H. P., & Curtis, P. S. (2008). Controls on annual forest carbon storage: Lessons from the past and predictions for the future. *Bioscience*, *58*, 609–622.

Hall, R. J., Skakun, R. S., Arsenault, E. J., & Case, B. S. (2006). Modeling forest stand structure attributes using Landsat ETM+ data: Application to mapping of aboveground biomass and stand volume. *Forest Ecology and Management*, *225*, 378–390.

Hall, F. G., Bergen, K., Blair, J. B., Dubayah, R., Houghton, R., Hurtt, G., et al. (2011). Characterizing 3D vegetation structure from space: Mission requirements. *Remote Sensing of Environment*, *115*, 2753–2775.

Harmon, M. E., Franklin, J. F., Swanson, F. J., Sollins, P., Gregory, S. V., Lattin, J. D., Anderson, N. H., Cline, S. P., Aumen, N. G., Sedell, J. R., Lienkaemper, G. W., Cromack, K., & Cummins, K. W. (1986). Ecology of coarse woody debris in temperate ecosystems. *Advances in Ecological Research*, *15*, 133–302.

Harmon, M. E., Ferrell, W. K., & Franklin, J. F. (1990). Effects on Carbon Storage of Conversion of Old-Growth Forests to Young Forests. *Science*, *247*, 699–702.

Harmon, M. E., & Sexton, J. M. (1996). Guidelines for measurements of woody detritus in forest ecosystems. *U.S. Long Term Ecological Research Program Network*, *20*, Albuquerque, NM.

Hay, C. M. (1991). Landsat Satellite Calibration Information Relating To The Tasseled Cap Transformation. unpublished.

Healey, S. P., Cohen, W. B., Yang, Z. Q., & Krankina, O. N. (2005). Comparison of Tasseled Cap-based Landsat data structures for use in forest disturbance detection. *Remote Sensing of Environment*, *97*, 301–310.

Healey, S. P., Cohen, W. B., Spies, T. A., Moeur, M., Pflugmacher, D., Whitley, M. G., & Lefsky, M. (2008). The Relative impact of harvest and fire upon landscape-level dynamics of older forests: Lessons from the Northwest Forest Plan. *Ecosystems*, *11*, 1106–1119.

Helmer, E. H., Ruzycki, T. S., Wunderle, J. M., Vogesser, S., Ruefenacht, B., Kwit, C., Brandeis, T. J., & Ewert, D. N. (2010). Mapping tropical dry forest height, foliage height profiles and disturbance type and age with a time series of cloud-cleared Landsat and ALI image mosaics to characterize avian habitat. *Remote Sensing of Environment*, *114*, 2457–2473.

Hostert, P., Roder, A., & Hill, J. (2003). Coupling spectral unmixing and trend analysis for monitoring of long-term vegetation dynamics in Mediterranean rangelands. *Remote Sensing of Environment*, *87*, 183–197.

Houghton, R. A. (2005). Aboveground forest biomass and the global carbon balance. *Global Change Biology*, *11*, 945–958.

Huang, C., Wylie, B., Homer, C., Yang, L., & Zylstra, G. (2002). Derivation of a tasselled cap transformation based on Landsat 7 at-satellite reflectance. *International Journal of Remote Sensing*, *23*, 1741–1748.

Huang, C. Q., Coward, S. N., Masek, J. G., Thomas, N., Zhu, Z. L., & Vogelmann, J. E. (2010). An automated approach for reconstructing recent forest disturbance history using dense Landsat time series stacks. *Remote Sensing of Environment*, *114*, 183–198.

Hudak, A. T., Lefsky, M. A., Cohen, W. B., & Berterretche, M. (2002). Integration of lidar and Landsat ETM plus data for estimating and mapping forest canopy height. *Remote Sensing of Environment*, *82*, 397–416.

Hudak, A. T., Crookston, N. L., Evans, J. S., Falkowski, M. J., Smith, A. M. S., Gessler, P. E., & Morgan, P. (2006). Regression modeling and mapping of coniferous forest basal area and tree density from discrete-return lidar and multispectral satellite data. *Canadian Journal of Remote Sensing*, *32*, 126–138.

Hudak, A. T., Crookston, N. L., Evans, J. S., Hall, D. E., & Falkowski, M. J. (2008). Nearest neighbor imputation of species-level, plot-scale forest structure attributes from LiDAR data. *Remote Sensing of Environment*, *112*, 2232–2245.

Jackson, R. D. (1983). Spectral indices in N-Space. *Remote Sensing of Environment*, *13*, 409–421.

Jakubauskas, M. E. (1996). Thematic Mapper characterization of lodgepole pine seral stages in Yellowstone National Park, USA. *Remote Sensing of Environment*, *56*, 118–132.

Jenkins, J. C., Chojnacky, D. C., Heath, L. S., & Birdsey, R. A. (2003). National-scale biomass estimators for United States tree species. *Forest Science*, *49*, 12–35.

Kauth, R. J., & Thomas, G. S. (1976). The tasseled cap — A graphic description of the spectral-temporal development of agricultural crops as seen by LANDSAT. *Symposium on Machine Processing of Remotely Sensed Data*. Indiana, USA: Purdue University of West Lafayette pp. pp. 4B-41 to 44B-51.

Kauth, R. J., Lambeck, P. F., Richardson, W., Thomas, G. S., & Pentland, A. P. (1979). Feature extraction applied to agricultural crops as seen by Landsat. *Technical session LACIE symposium* (pp. 705–721). Houston: National Aeronautics and Space Administration.

Kennedy, R. E., & Cohen, W. B. (2003). Automated designation of tie-points for image-to-image coregistration. *International Journal of Remote Sensing*, *24*, 3467–3490.

Kennedy, R. E., Cohen, W. B., & Schroeder, T. A. (2007). Trajectory-based change detection for automated characterization of forest disturbance dynamics. *Remote Sensing of Environment*, *110*, 370–386.

Kennedy, R. E., Cohen, W. B., Kirschbaum, A. A., & Haunreiter, E. (2007). Protocol for Landsat-based monitoring of landscape dynamics at North Coast and Cascades Network parks. *U.S. geological survey techniques and methods*. : USGS Biological Resources Division. U.S. Geological Survey http://pubs.usgs.gov/tm/2007/tm2g1/:

Kennedy, R. S. H., Spies, T. A., & Gregory, M. J. (2008). Relationships of dead wood patterns with biophysical characteristics and ownership according to scale in Coastal Oregon, USA. *Landscape Ecology*, *23*, 55–68.

Kennedy, R. E., Yang, Z., & Cohen, W. B. (2010). Detecting trends in forest disturbance and recovery using yearly Landsat time series: 1, LandTrendr — Temporal segmentation algorithms. *Remote Sensing of Environment*, *114*, 2897–2910.

Kennedy, R. E., Yang, Z., Cohen, W. B., Pfaff, E., Braaten, J., & Nelson, P. (2012). Spatial and temporal patterns of forest disturbance and growth within the area of the Northwest Forest Plan. *Remote Sensing of Environment*, *122*, 117–133.

Key, C. H., & Benson, N. C. (2005). Landscape assessment: Remote sensing of severity, the Normalized Burn Ratio. In D. C. Lutes (Ed.), *FIREMON: Fire effects monitoring and inventory system, General Technical Report, RMRS-GTR-164-CD: LA1-LA51*. Ogden, UT: USDA Forest Service, Rocky Mountain Research Station.

Kim, Y., Yang, Z. Q., Cohen, W. B., Pflugmacher, D., Lauver, C. L., & Vankat, J. L. (2009). Distinguishing between live and dead standing tree biomass on the North Rim of Grand Canyon National Park, USA using small-footprint lidar data. *Remote Sensing of Environment*, *113*, 2499–2510.

Korpela, I., Orka, H. O., Hyyppa, J., Heikkinen, V., & Tokola, T. (2010). Range and AGC normalization in airborne discrete-return LiDAR intensity data for forest canopies. *ISPRS Journal of Photogrammetry and Remote Sensing*, *65*, 369–379.

Kuemmerle, T., Chaskovskyy, O., Knorn, J., Radeloff, V. C., Kruhlov, I., Keeton, W. S., & Hostert, P. (2009). Forest cover change and illegal logging in the Ukrainian Carpathians in the transition period from 1988 to 2007. *Remote Sensing of Environment*, *113*, 1194–1207.

Landsberg, J. J., & Waring, R. H. (1997). A generalised model of forest productivity using simplified concepts of radiation-use efficiency, carbon balance and partitioning. *Forest Ecology and Management*, *95*, 209–228.

Lawrence, R. L., & Ripple, W. J. (2000). Fifteen years of revegetation of Mount St, Helens: A landscape-scale analysis. *Ecology*, *81*, 2742–2752.

Lefsky, M. A., Cohen, W. B., Acker, S. A., Parker, G. G., Spies, T. A., & Harding, D. (1999). Lidar remote sensing of the canopy structure and biophysical properties of Douglas-fir western hemlock forests. *Remote Sensing of Environment*, *70*, 339–361.

Lefsky, M. A., Cohen, W. B., Parker, G. G., & Harding, D. J. (2002). Lidar remote sensing for ecosystem studies. *Bioscience*, *52*, 19–30.

Lefsky, M. A., Hudak, A. T., Cohen, W. B., & Acker, S. A. (2005). Geographic variability in lidar predictions of forest stand structure in the Pacific Northwest. *Remote Sensing of Environment*, *95*, 532–548.

Lefsky, M. A., Turner, D. P., Guzy, M., & Cohen, W. B. (2005). Combining lidar estimates of aboveground biomass and Landsat estimates of stand age for spatially extensive validation of modeled forest productivity. *Remote Sensing of Environment*, *95*, 549–558.

Lobser, S. E., & Cohen, W. B. (2007). MODIS tasselled cap: Land cover characteristics expressed through transformed MODIS data. *International Journal of Remote Sensing*, *28*, 5079–5101.

Lorey, T. (1878). Die mittlere Bestandeshoehe. *Allgemeine Forst- und Jagdzeitung*, *54*, 149–155.

Lu, D. S. (2006). The potential and challenge of remote sensing-based biomass estimation. *International Journal of Remote Sensing*, *27*, 1297–1328.

Lumley, T. (2009). *Leaps: Regression subset selection.* : R Foundation for Statistical Computing.

Lunetta, R., Johnson, D. M., Lyon, J., & Crotwell, J. (2004). Impacts of imagery temporal frequency on land-cover change detection monitoring. *Remote Sensing of Environment*, *89*, 444–454.

Malila, W. A. (1980). Change vector analysis: An approach for detecting forest changes with Landsat. *Proceedings of the 6th Annual Symposium on Machine Processing of Remotely Sensed Data, 03–06 June* (pp. 326–335). West Lafayette, Indiana: Purdue University.

Mallows, C. L. (1973). Some comments on Cp. *Technometrics*, *15*, 661–667.

Markham, B. L., & Barker, J. L. (1986). Landsat MSS and TM post-calibration dynamic ranges, exoatmospheric reflectances and at-satellite temperatures. *Earth Observation Satellite Co. Lanham, MD*.

Masek, J. G., Huang, C. Q., Wolfe, R., Cohen, W., Hall, F., Kutler, J., & Nelson, P. (2008). North American forest disturbance mapped from a decadal Landsat record. *Remote Sensing of Environment*, *112*, 2914–2926.

Meigs, G. W., Kennedy, R. E., & Cohen, W. B. (2011). A Landsat time series approach to characterize bark beetle and defoliator impacts on tree mortality and surface fuels in conifer forests. *Remote Sensing of Environment*, *115*, 3707–3718.

Moore, J. A., Zhang, L., & Stuck, D. (1996). Height-Diameter Equations for Ten Tree Species in the Inland Northwest. *Western Journal of Applied Forestry*, *11*, 132–137.

Morsdorf, F., Mårell, A., Koetz, B., Cassagne, N., Pimont, F., Rigolot, E., et al. (2010). Discrimination of vegetation strata in a multi-layered Mediterranean forest ecosystem using height and intensity information derived from airborne laser scanning. *Remote Sensing of Environment*, *114*, 1403–1415.

Muss, J. D., Mladenoff, D. J., & Townsend, P. A. (2011). A pseudo-waveform technique to assess forest structure using discrete lidar data. *Remote Sensing of Environment*, *115*, 824–835.

O'hara, K. L. (2001). The silviculture of transformation — A commentary. *Forest Ecology and Management*, *151*, 81–86.

Parris, T., & Rice, D. (1983, August). Appendix A: Presentation of known between-satellite calibration transforms among Landsats 1 through 4. In D. P. Rice, & W. A. Malila (Eds.), *Final Report: Investigation of Radiometric Properties of the Landsat-4 Multispectral Scanner. Nasa Contract #NAS5-27254* (pp. 48107). Ann Arbor, MI: Environmental Research Institute of Michigan.

Parker, T. J., Clancy, K. M., & Mathiasen, R. L. (2006). Interactions among fire, insects and pathogens in coniferous forests of the interior western United States and Canada. *Agricultural and Forest Entomology*, *8*, 167–189.

Pesonen, A., Maltamo, M., Eerikainen, K., & Packalen, P. (2008). Airborne laser scanning-based prediction of coarse woody debris volumes in a conservation area. *Forest Ecology and Management*, *255*, 3288–3296.

Peterson, U., & Nilson, T. (1993). Successional reflectance trajectories in northern temperate forests. *International Journal of Remote Sensing*, *14*(3), 609–613.

Powell, S. L., Cohen, W. B., Yang, Z., Pierce, J. D., & Alberti, M. (2008). Quantification of impervious surface in the Snohomish Water Resources Inventory Area of Western Washington from 1972–2006. *Remote Sensing of Environment*, *112*, 1895–1908.

Powell, S. L., Cohen, W. B., Healey, S. P., Kennedy, R. E., Moisen, G. G., Pierce, K. B., & Ohmann, J. L. (2010). Quantification of live aboveground forest biomass dynamics with Landsat time-series and field inventory data: A comparison of empirical modeling approaches. *Remote Sensing of Environment*, *114*, 1053–1068.

R Development Core Team (2011). R: A language and environment for statistical computing. *R foundation for statistical computing*. Vienna, Austria: R Foundation for Statistical Computing ISBN 3-900051-07-0, URL http://www.R-project.org/.

Roder, A., Hill, J., Duguy, B., Alloza, J. A., & Vallejo, R. (2008). Using long time series of Landsat data to monitor fire events and post-fire dynamics and identify driving factors. A case study in the Ayora region (eastern Spain). *Remote Sensing of Environment*, *112*, 259–273.

Schoennagel, T., Veblen, T. T., & Romme, W. H. (2004). The interaction of fire, fuels, and climate across rocky mountain forests. *Bioscience*, *54*, 661–676.

Schroeder, T. A., Cohen, W. B., Song, C., Canty, M. J., & Yang, Z. (2006). Radiometric correction of multi-temporal Landsat data for characterization of early successional forest patterns in western Oregon. *Remote Sensing of Environment*, *103*, 16–26.

Schroeder, T. A., Cohen, W. B., & Yang, Z. Q. (2007). Patterns of forest regrowth following clearcutting in western Oregon as determined from a Landsat time-series. *Forest Ecology and Management*, *243*, 259–273.

Schroeder, T. A., Wulder, M. A., Healey, S. P., & Moisen, G. G. (2011). Mapping wildfire and clearcut harvest disturbances in boreal forests with Landsat time series data. *Remote Sensing of Environment*, *115*, 1421–1433.

Smith, J. E., Heath, L. S., & Jenkins, J. C. (2003). *Forest volume-to-biomass models and estimates of mass for live and standing dead trees of U.S. forests.* Gen. Tech. Rep. NE-298. Newtown Square, PA: U.S. Department of Agriculture, Forest Service, Northeastern Research Station 57 pp.

Sonnenschein, R., Kuemmerle, T., Udelhoven, T., Stellmes, M., & Hostert, P. (2011). Differences in Landsat-based trend analyses in drylands due to the choice of vegetation estimate. *Remote Sensing of Environment*, *115*, 1408–1420.

Spies, T. A., Johnson, K. N., Burnett, K. M., Ohmann, J. L., McComb, B. C., Reeves, G. H., Bettinger, P., Kline, J. D., & Garber-Yonts, B. (2007). Cumulative ecological and socioeconomic effects of forest policies in Coastal Oregon. *Ecological Applications*, *17*, 5–17.

Spies, T. A. (1998). Forest structure: A key to the ecosystem. *Northwest Science*, *72*, 34–39.

Thompson, D. R., & Wehmanen, O. A. (1980). Using Landsat digital data to detect moisture stress in corn-soybean growing regions. *Photogrammetric Engineering and Remote Sensing*, *46*, 1087–1093.

Thornton, P. E., Law, B. E., Gholz, H. L., Clark, K. L., Falge, E., Ellsworth, D. S., Golstein, A. H., Monson, R. K., Hollinger, D., Falk, M., Chen, J., & Sparks, J. P. (2002). Modeling and measuring the effects of disturbance history and climate on carbon and water budgets in evergreen needleleaf forests. *Agricultural and Forest Meteorology*, *113*, 185–222.

Townshend, J. R. G., Justice, C. O., Gurney, C., & McManus, J. (1992). The impact of misregistration on change detection. *IEEE Transactions on Geoscience and Remote Sensing*, *30*(5), 1054–1060.

Treuhaft, R. N., Law, B. E., & Asner, G. P. (2004). Forest attributes from radar interferometric structure and its fusion with optical remote sensing. *Bioscience*, *54*, 561–571.

Turner, D. P., Cohen, W. B., Kennedy, R. E., Fassnacht, K. S., & Briggs, J. M. (1999). Relationships between leaf area index and Landsat TM spectral vegetation indices across three temperate zone sites. *Remote Sensing of Environment*, *70*, 52–68.

Van Wagner, C. E. (1968). The line intersect method in forest fuel sampling. *Forest Science*, *14*, 20–26.

Waddell, K. L. (2002). Sampling coarse woody debris for multiple attributes in extensive resource inventories. *Ecological Indicators*, *1*, 139–153.

Warren, W. G., & Olsen, P. F. (1964). A line intersect technique for assessing logging waste. *Forest Science*, *10*, 267–276.

Woodcock, C. E., Allen, R., Anderson, M., Belward, A., Bindschadler, R., Cohen, W., Gao, F., Goward, S. N., Helder, D., Helmer, E., Nemani, R., Oreopoulos, L., Schott, J., Thenkabail, P. S., Vermote, E. F., Vogelmann, J., Wulder, M. A., Wynne, R., & Team, L. S. (2008). Free access to Landsat imagery. *Science*, *320*, 1011.

Wulder, A. A., Skakun, R. S., Kurz, W. A., & White, J. C. (2004). Estimating time since forest harvest using segmented Landsat ETM + imagery. *Remote Sensing of Environment*, *93*, 179–187.

Wulder, M. A., & Seemann, D. (2003). Forest inventory height update through the integration of lidar data with segmented Landsat imagery. *Canadian Journal of Remote Sensing*, *29*, 536–543.

Wulder, M. A., Skakun, R. S., Dymond, C. C., Kurz, W. A., & White, J. C. (2005). Characterization of the diminishing accuracy in detecting forest insect damage over time. *Canadian Journal of Remote Sensing*, *31*, 421–431.

Wulder, M. A., White, J. C., Alvarez, F., Han, T., Rogan, J., & Hawkes, B. (2009). Characterizing boreal forest wildfire with multi-temporal Landsat and LIDAR data. *Remote Sensing of Environment*, *113*, 1540–1555.

Yang, Z. Q., Cohen, W. B., & Harmon, M. E. (2005). Modeling early forest succession following clear-cutting in western Oregon. *Canadian Journal of Forest Research-Revue Canadienne De Recherche Forestiere*, *35*, 1889–1900.

Zhao, K. G., & Popescu, S. (2009). Lidar-based mapping of leaf area index and its use for validating GLOBCARBON satellite LAI product in a temperate forest of the southern USA. *Remote Sensing of Environment*, *113*, 1628–1645.